THE JOURNAL OF PHYSICAL CHEMISTRY C

Article

pubs.acs.org/JPCC

Stable, Single-Layer MX_2 Transition-Metal Oxides and Dichalcogenides in a Honeycomb-Like Structure

C. Ataca,[†,‡,§] H. Şahin,[‡,§] and S. Ciraci*[,†,‡,§]

[†]Department of Physics, [‡]Institute of Materials Science and Nanotechnology, and [§]UNAM-National Nanotechnology Research Center, Bilkent University, Ankara 06800, Turkey

ABSTRACT: Recent studies have revealed that single-layer transition-metal oxides and dichalcogenides (MX_2) might offer properties superior to those of graphene. So far, only very few MX_2 compounds have been synthesized as suspended single layers, and some of them have been exfoliated as thin sheets. Using first-principles structure optimization and phonon calculations based on density functional theory, we predict that, out of 88 different combinations of MX_2 compounds, several of them can be stable in free-standing, single-layer honeycomb-like structures. These materials have two-dimensional hexagonal lattices and have top-view appearances as if they consisted of either honeycombs or centered honeycombs. However, their bonding is different from that of graphene; they can be viewed as a positively charged plane of transition-metal atoms sandwiched between two planes of negatively charged oxygen or chalcogen atoms. Electron correlation in transition-metal oxides was treated by including Coulomb repulsion through LDA + U calculations. Our analysis of stability was extended to include in-plane stiffness, as well as ab initio, finite-temperature molecular dynamics calculations. Some of these single-layer structures are direct- or indirect-band-gap semiconductors, only one compound is half-metal, and the rest are either ferromagnetic or nonmagnetic metals. Because of their surface polarity, band gap, high in-plane stiffness, and suitability for functionalization by adatoms or vacancies, these single-layer structures can be utilized in a wide range of technological applications, especially as nanoscale coatings for surfaces contributing crucial functionalities. In particular, the manifold WX_2 heralds exceptional properties promising future nanoscale applications.

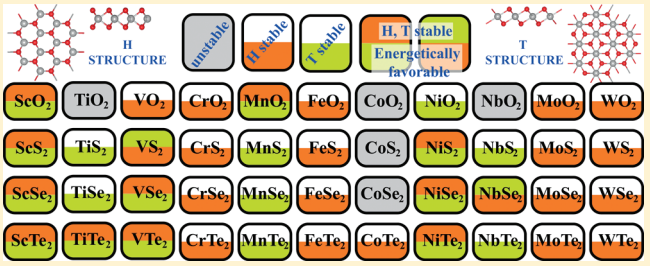

INTRODUCTION

Three-dimensional (3D) MX_2 (M, transition metal; X, chalcogen atom) compounds constitute one of the most interesting classes of materials and display a wide range of important properties. Their bulk compounds include oxide superconductors,[1] half-metallic magnets,[2] superlubricants,[3] catalysts in redox-based reactions,[4] and solar converters,[5] among others. Some of these compounds have D_{6h} point-group symmetry and occur in layered structures formed by the stacking of weakly interacting two-dimensional (2D) MX_2 layers and are specified as 2H-MX_2. Another type of layered structure known as the 1T structure has D_{3d} point-group symmetry and is common to several of MX_2 compounds. Only a few 3D MX_2 compounds can be stable both in 2H and 1T structures. In addition to 2H and 1T layered structures, some MX_2 compounds can be stable in one of the 3D structures known as rutile, 3R, marcasite, anatase, pyrite, and tetragonal structures. An extensive review of bulk 3D MX_2 compounds can be found in ref 6.

Specifically, rutile crystal and thin films of CrO_2 have been investigated because of their spintronic applications. Tunneling magnetoresistance was initially observed in films of half-metallic CrO_2.[7] Electronic and magnetic properties of bulk[8] and epitaxial[9] CrO_2 have also been investigated theoretically.[10] Single-layer CoO_2 has played an important role in understanding the superconducting properties of nickel and cobalt oxide based compounds. In these structures, single layers of CoO_2 are separated generally by thick insulating layers of Na^+ ions and H_2O molecules.[1] The high-T_C superconducting properties of these structures arise from the single layer of the CoO_2 plane. Electronic, magnetic, and optical properties of the cubic pyrite-type CoS_2 structure have been investigated theoretically,[2,11−14] focusing on the half-metallic properties of this magnet.

VO_2 has various allotropes at different temperatures. For example, at low temperature, a monoclinic (M1) phase occurs, whereas at high temperatures, the rutile metallic phase is favored. By varying the temperature of the system, one can observe the metal-to-insulator transition.[15] The synthesis and characterization of the layered structure of bulk VSe_2 and its superconducting properties have also been investigated experimentally.[16,17] A recent theoretical study on the electronic and magnetic properties of monolayers of VS_2 and VSe_2[18] concluded that the magnetic properties of these structures can be controlled by applying strain.

The interaction of iron with chalcogens, and specifically with O_2 molecules, is of great interest, because it involves processes varying from corrosion to oxygen transport in biological

Received: December 29, 2011
Revised: March 18, 2012
Published: March 23, 2012

systems. Such materials can also be used as catalysts or catalytic supports in redox-based reactions.[4] FeS_2, the most well-known compound among Fe-based materials, has been studied extensively. The pyrite structure, the most stable polymorph of FeS_2, is a crucial compound in materials research.[19−23] Recently, a new method has been put forward and used to synthesize 2D nanowire networks of FeS_2.[24] Powders of FeS_2 showing rodlike morphologies are attracting considerable interest, because they are promising materials for solar energy conversion. The shape and thermodynamic stability of FeS_2 powders have been investigated using first-principles methods, pointing out the differences between nano- and macroscale properties.[25] FeS_2 nanosheets on iron substrates are also used as photocathodes from tandem dye-sensitized solar cells.[26] FeS_2 pyrite nanocrystal inks are also used in thin-film photovoltaic solar cells.[5] The above brief overview intends to show how comprehensive and diverse the features of MX_2 crystals can be.

On the other hand, advances in nanotechnology have led to the synthesis of novel 2D nanostructures. For example, exceptional properties, such as high carrier mobility, linearly crossing bands at the Fermi level contributing massless Fermion behavior, and perfect electron−hole symmetry that originates from a strictly 2D honeycomb structure, have made graphene an attractive material for future applications.[27,28] Group IV elements, such as Si and Ge, have also been shown to form buckled honeycomb structures with bands linearly crossing at the Fermi level.[29−32] In addition, suspended 2D single-layer BN[33] and, more recently, single-layer transition-metal dichalcogenides MoS_2[34] and WS_2[35] with honeycomb structure have been synthesized. Single-layer $NbSe_2$ was synthesized only on SiO_2 substrate.[36] Theoretical[37−45] and experimental studies dealing with the electronic structure,[34,40] lattice dynamics, Raman spectrum[46,47] and Born effective charges indicate that single-layer MoS_2 is a nonmagnetic semiconductor displaying exceptional properties. These properties of single-layer MoS_2 and its nanoribbons[41] have been exploited in diverse fields such as nanotribology,[3,48] hydrogen production,[49] hydrodesulfurization,[50] and solar energy production.[51] Whereas the charged surfaces of MoS_2 attain a water-repellant character, specific vacancy defects in MoS_2 can split H_2O to produce free H_2 molecule as a sustainable energy resource.[52] Most recently, a transistor fabricated from a single MoS_2 layer pointed out features of these materials that can be superior to those of graphene.[53] Whereas graphene is ideal for fast analog circuits, single-layer MoS_2 appears to be promising for optoelectronic devices, solar cells, and light-emitting diodes.

The most recent experimental study by Coleman et al.,[54] which reported liquid exfoliation of MoS_2, WS_2, $MoSe_2$, $TaSe_2$, $NbSe_2$, $NiTe_2$, and $MoTe_2$ nanosheets having honeycomb-like structures, motivated us to engage in an extensive analysis of stability to address the question of whether other single-layer transition-metal dioxides or dichalcogenides MX_2 can exist in honeycomb-like structures. In this work, we examined MX_2 compounds (M = Sc, Ti, V, Cr, Mn, Fe, Co, Ni, Nb, Mo, W; X = O, S, Se, Te) to reveal which ones can be stable in 2D suspended, single-layer structure. We took into account two different single-layer structures, namely, honeycomb (H) and centered honeycomb (T) structures; both can be viewed as a positively charged 2D hexagonal lattice of M atoms sandwiched between two hexagonal lattices of negatively charged X atoms. In both H and T structures, instead of forming covalent sp^2 bonding with three neighboring carbon atoms in graphene, each M atom has six nearest X atoms, and each X atom has three nearest M atoms forming p−d hybridized ionic M−X bonds. Figures 1 and 2 depict 2D single-layer H and T

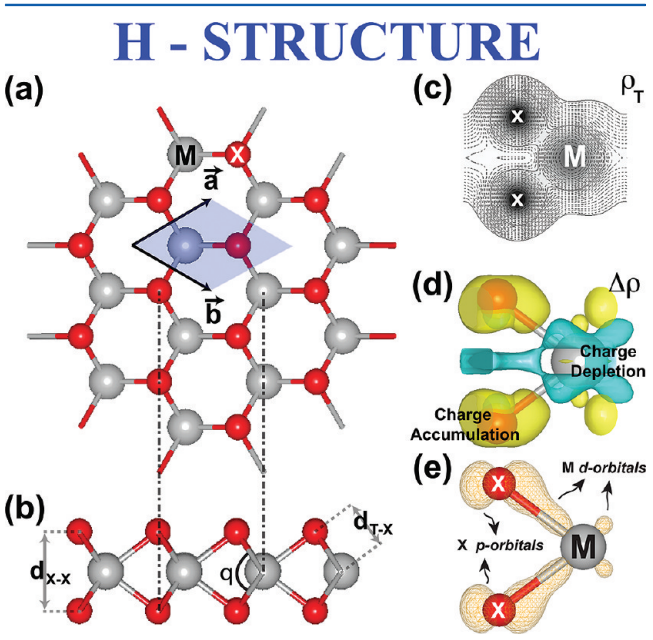

Figure 1. Atomic structure and charge density analysis of 2D single-layer MoO_2 presented as a prototype for MX_2 in the H structure. (a) Top and (b) side views of H structure showing the primitive unit cell of the 2D hexagonal lattice with Bravais lattice vectors $\vec{a}$ and $\vec{b}$ ($|\vec{a}| = |\vec{b}|$) and relevant internal structural parameters. Gray and red balls indicate metal (M) and oxygen (X = O) atoms, respectively. (c) Contour plots of the total charge density, ρ_T. (d) Isosurfaces of difference charge density, $\Delta\rho$. Turquoise and yellow regions indicate depletion and accumulation of electrons, respectively. (e) Charge density isosurfaces showing p−d hybridization in the Mo−O bond. The isosurface value is taken as 0.01 electron/Å^3. In the top view in panel a, unlike in graphene, M and X_2 occupy alternating corners of a hexagon.

structures, together with their hexagonal unit cells, contour plots of the total charge density ρ_T, and isosurfaces of difference charge density $\Delta\rho$ (where charges of free atoms situated at the optimized crystal structure are subtracted from ρ_T).

Based on extensive stability analysis using first-principles calculations of structure optimization, phonon frequency, formation energy, elastic properties, and finite-temperature ab initio molecular dynamics (MD) calculations, we predict that, out of 88 different MX_2 compounds, 52 different stable 2D single-layer H and/or T structures can occur as free-standing. Because of the instability occurring in long-wavelength acoustical modes, a few of them can be stable only at small size. Our results are summarized in Figure 3. The series of MX_2 compounds with M = Cr, Mo, and W and X = O, S, Se, and Te are nonmagnetic semiconductors in the H structure. On the other hand, the series with M = V, Mn, and Fe are ferromagnetic metals with a net magnetic moment (ranging from 0.2 to 3.0 μ_B per cell). Three-dimensional 2H-$NbSe_2$ has metallic and stable H structure in two dimensions, except for some instability in very-long-wavelength acoustical waves. Moreover, $NbSe_2$ also has a free-standing and stable T structure with a slightly higher energy. Interestingly, NiS_2 and $NiSe_2$ are metallic in the H structure, but become semiconductor in the T structure. Whereas some of these single-layer compounds in Figure 3 appear to survive up to high

dx.doi.org/10.1021/jp212558p | J. Phys. Chem. C 2012, 116, 8983−8999

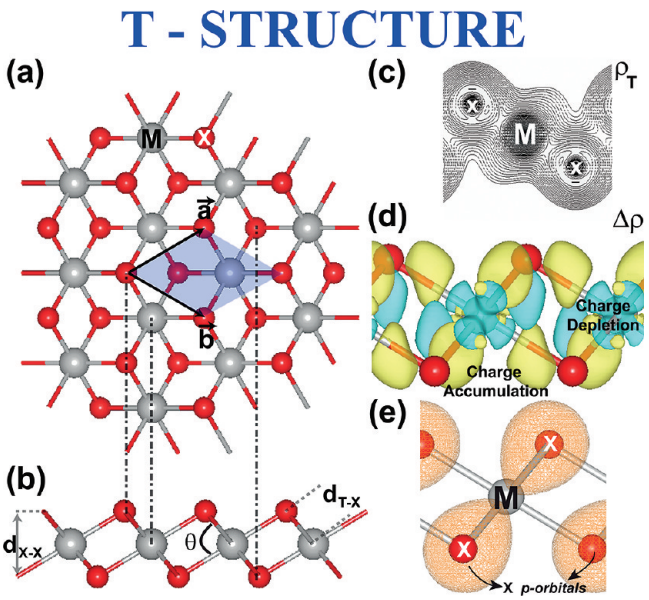

Figure 2. Atomic structure and charge density analysis of 2D single-layer NiS_2 presented as a prototype for MX_2 in the T structure. (a) Top and (b) side views of T structure showing the primitive unit cell of the 2D hexagonal lattice with Bravais lattice vectors $\vec{a}$ and $\vec{b}$ ($|\vec{a}| = |\vec{b}|$) and relevant internal structural parameters. (c) Contour plots of the total charge density, ρ_T. (d) Isosurfaces of difference charge density, $\Delta\rho$. Turquoise and yellow regions indicate depletion and accumulation of electrons, respectively. (e) Charge density isosurfaces showing Ni−S bonds. The isosurface value is taken as 0.01 electron/Å^3. In the top view in panel a, whereas one of the two X atoms occupies alternating corners of a regular hexagon, the second X atom is displaced by $(\vec{a} + \vec{b})/3$ to occupy the centers of the adjacent hexagons.

temperatures, some of them are expected to become unstable as their temperatures are raised. Transition-metal oxides such as TiO_2, CoO_2, and NbO_2 and CoS_2 and $CoSe_2$ are found to be unstable in both the H and T structures. However, these single-layer MX_2 compounds could be stable if they were placed on specific substrates. All of these structures display interesting electronic, magnetic, and mechanical properties and have trends correlated with the electronegativity of constituent elements X and M.

Although it is relatively easy for 2D single-layer MX_2 structures to be exfoliated from parent 3D layered 2H-MX_2 or 1T-MX_2 structures, it is not obvious whether stable single layers can form if the parent 3D crystal is not layered. Following this simple methodology, by searching only the existence of parent 3D layered 2H-MX_2 structure from the Landolt−Bornstein database,[55] Ding et al.[56] reported that $MoSe_2$, $MoTe_2$, $NbSe_2$, WS_2, WSe_2, TaS_2, and $TaSe_2$ can have monolayer H structures and reported their electronic properties. Nonetheless, recent experimental and theoretical studies indicating that silicene,[30,57−61] III−V compounds,[31] SiC,[62] and ZnO[63−65] 2D single layers all have honeycomb structures even though their parent 3D bulk materials are not layered provide strong reasons for pursuing our analysis to search for single-layer MX_2 compounds. The intention of this work was to attract interest in the manifold of single-layer MX_2 compounds by showing how they can provide a wide range of options in materials research. Accordingly, rather than providing an in-depth analysis, our discussion is focused on the broad properties and various classes of MX_2 compounds showing similar trends.

METHOD

Our stability analysis and calculation of physical properties were carried out using first-principles plane-wave calculations within density functional theory (DFT) and projector-augmented-wave (PAW) potentials.[66] The exchange correlation potential was represented by the local density approximation[67] (LDA) for both spin-polarized and spin-unpolarized cases. In addition, our results were tested using the generalized gradient approximation[68] with the van der Waals correction.[69,70] All structures were treated using periodic boundary conditions. Because the electrons of some transition-metal oxides are strongly correlated, they might not be represented properly by DFT. Thus, to correct for the deficiencies of DFT, we also carried out LDA + U calculations.[71] All values calculated in this article were obtained using LDA unless stated otherwise.

Supercell size, kinetic energy cutoff, and Brillouin-zone (BZ) sampling of the calculations were determined after extensive convergence analysis. A large spacing of ∼15 Å between 2D single layers of MX_2 was used to prevent interlayer interactions. A plane-wave basis set with kinetic energy cutoff of 520 eV was used. In the self-consistent-field potential and total energy calculations, the BZ was sampled by special **k** points.[72] The numbers of these **k** points were $(37 \times 37 \times 1)$ for the primitive MX_2 unit cell and were scaled according to the size of the supercells. All atomic positions and lattice constants were optimized using the conjugate gradient method, where the total energy and atomic forces were minimized. The convergence for energy was chosen as 10^{-6} eV between two consecutive steps, and the maximum Hellmann−Feynman forces acting on each atom were reduced to a value of less than 0.01 eV/Å upon ionic relaxation. The pressure in the unit cell was kept below 1 kbar.

Bader analysis is used to calculate the charge on atoms.[73] Because LDA is designed to describe systems with slowly varying electron densities and can fail to model localized d orbitals, more accurate electronic structure calculations were carried out using the screened-nonlocal-exchange Heyd−Scuseria−Ernzerhof (HSE) functional of the generalized Kohn−Sham scheme[74,75] for specific structures. Frequency-dependent GW_0 calculations[76] were carried out to correct the LDA band gaps. However, whereas the GW_0 correction was successful in predicting 3D bulk MoS_2, it seems to have overestimated the band gap of 2D MoS_2 in the H structure.[42] This surprising situation, which is discussed later in the text, requires further analysis. Numerical calculations were performed using VASP.[77,78] The phonon dispersion curves and Raman-active modes were calculated using the small-displacement method (SDM)[79] with VASP. For critical situations, phonon calculations based on the plane-wave self-consistent-field (PWSCF) method[81] were also performed to carry out the analysis of Raman- and infrared-active phonon modes and check specific results.

STABILITY ANALYSIS

MX_2 compounds have diverse 3D crystal structures in different space groups, as presented in Table 1. Among these, the 2H and 1T structures are layered, and hence, like graphite, they are formed by stacking of specific layers. The structures of the remaining MX_2 compounds are not layered. The focus of our study was to determine which of the MX_2 compounds can form stable 2D single-layer structures. Our study considered only the structures having hexagonal lattices as shown in Figures 1 and 2. These are H structures (honeycombs) with D_{3h} point-group

dx.doi.org/10.1021/jp212558p | J. Phys. Chem. C 2012, 116, 8983−8999

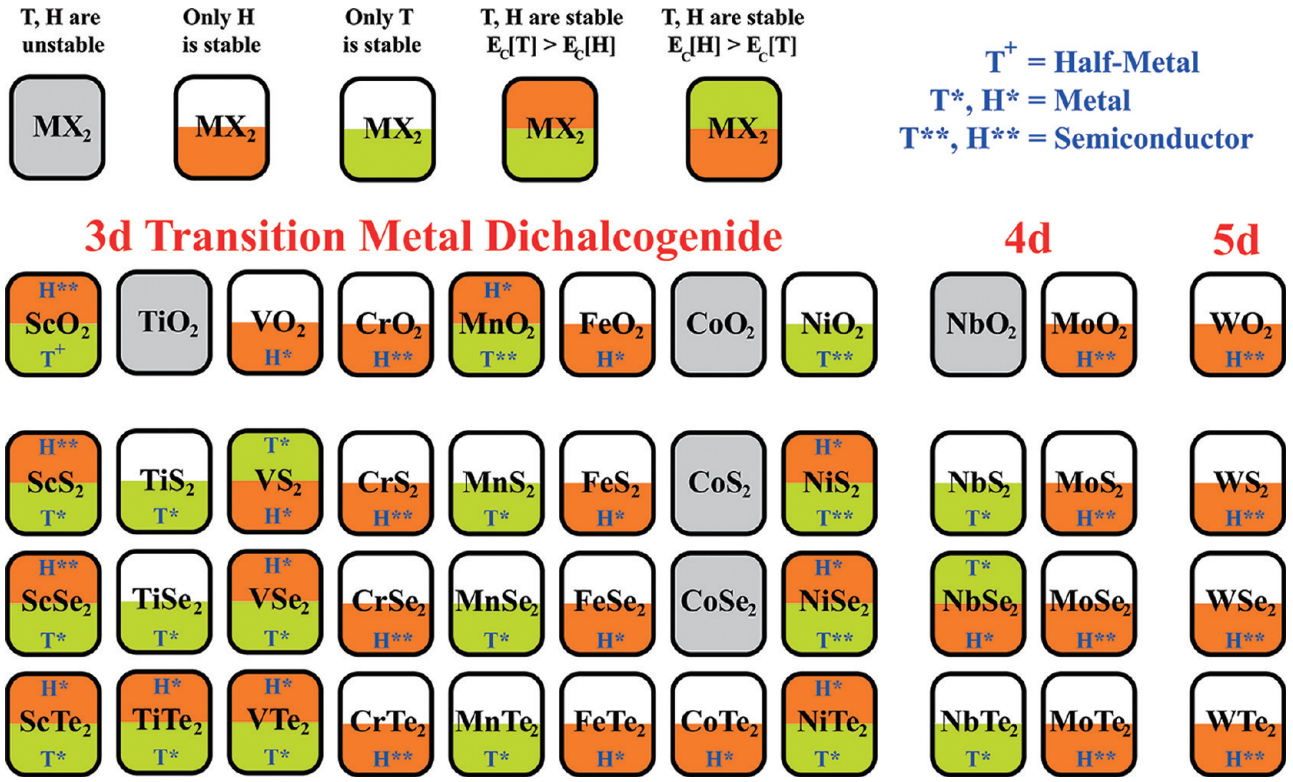

Figure 3. Summary of the results of our stability analysis comprising 44 different MX_2 compounds that can form stable, 2D single-layer H and/or T structures. Transition-metal atoms indicated by M are divided into 3d, 4d and 5d groups. MX_2 compounds shaded light gray form neither stable H nor T structure. In each box, the lower-lying structure (H or T) is the ground state. The resulting structures (T or H) can be half-metallic (+), metallic (*), or semiconducting (**).

symmetry and T structures (centered honeycombs) with C_{3v} symmetry. The formation of stable, single-layer MX_2 compounds on a sample specific substrate might be relatively easy, but it is beyond the scope of the present study. While this study was being performed, Ding et al.[56] investigated electronic and vibrational properties of single-layer MX_2 (M = Mo, Nb, W, Ta; X = S, Se, Te) in the H structure. The only reason they considered the H structure is because these compounds form stable 2H-MX_2 in 3D. Instead of providing tests of whether these 2D nanostructures are stable through the full spectrum of phonons and temperature-dependent ab initio MD calculations, they calculated the phonon frequencies only at the Γ point to reveal the Raman-active modes. Phonon dispersion spectrum analysis is an important indication of the stability of a system because phonon modes can become imaginary at other points in the BZ, when symmetry operations throughout DFT calculations are not taken into account correctly. Computationally, systems can be forced to have positive frequencies at the Γ point; however, this might not mean that they are stable. In our work, we carefully took into account the symmetry of the structure and calculated the full phonon dispersion of the structures. In this respect, the work by Ding et al.[56] had a scope different from that of the present article, and they apparently considered a small fraction of the manifold we treat here.

Structure Optimization. Our analysis of stability started by calculating the total energy of MX_2 compounds in the single-layer H and T structures depicted in Figures 1 and 2. Optimization was performed by minimizing the total energy and atomic forces by varying the atomic positions in the unit cell and the lattice constants. If a structure was stable, optimization usually converged to the structure. Furthermore, we calculated the cohesive energy relative to free constituent atoms. The cohesive energy per unit cell or per MX_2 unit was calculated using the expression $E_C = E_T[M] + 2E_T[X] - E_T[MX_2]$, in terms of the total energy of MX_2, $E_T[MX_2]$, and the total energies of free M and X atoms, $E_T[M]$ and $E_T[X]$, respectively. We found that the calculated cohesive energies were all positive and in the range of 10−20 eV, indicating a strong cohesion relative to free atoms of the constituents. Although a positive value of E_C alone is not sufficient to indicate whether a given MX_2 structure can form, the formation energy, E_f, is usually taken to be a good criterion. The formation energies E_f, which were obtained by subtracting the cohesive energies of the constituent elements in their equilibrium (bulk, liquid, or gas) phases, $E_C[M]$ and $E_C[X]$. Specifically, $E_f = E_C - E_C[M] - 2E_C[X]$. For the sake of comparison, we calculated E_f using both experimental cohesive energies[80] and calculated cohesive energies of the constituent elements. Calculated formation energies were positive for all H and T structures that were found to be stable as a result of a series of stability analyses.

The optimized lattice constants and other structure parameters of stable structures are also presented in Table 1. Experimental data on the lattice constants of MX_2 compounds in the H structure are not available yet. Even though the lattice constants of MoS_2 in the H structure (which is the most studied single-layer MX_2) have not been measured experimentally yet, they can be inferred from the lattice constants of 2H-MoS_2. Thus, the lattice constants of MoS_2 are expected to be close to those of 2H-MoS_2, which were measured to be $a = b =$ 3.16 Å. The LDA is known to predict overbinding and, hence, lattice constants that are slightly shorter than the experimental

dx.doi.org/10.1021/jp212558p | J. Phys. Chem. C 2012, 116, 8983−8999

Table 1. Calculated Values of Stable, Free-Standing, 2D Single-Layer MX_2 in the H and T Structures: Lateral Lattice Constants, $|\vec{a}| = |\vec{b}|$; Bond Lengths, d_{M-X} and d_{X-X}; X−M−X Bond Angles, θ; Cohesive Energies per MX_2 Unit, E_C; Formation Energies per MX_2 Unit, E_f;[a80] Energy Band Gaps, E_g; GW_0-Corrected Energy Band Gaps, $E_g^{GW_0}$;[b] Total Magnetic Moments in the Unit Cell, μ; Excess Charges on M Atoms, ρ_M;[c] Excess Charges on X Atoms, ρ_X;[d] In-Plane Stiffness Values, C; and 3D Bulk Structures of MX_2[e−g]

	type	a (Å)	d_{M-X} (Å)	d_{X-X} (Å)	θ (deg)	E_C (eV)	E_f (eV)	E_g (eV)	$E_g^{GW_0}$ (eV)	μ (μ_B)	ρ_M (electrons)	ρ_X (electrons)	C (N/m)	3D bulk structure[h]
ScO_2	H	3.16	2.09	2.04	58.30	20.35	7.83 (11.25)	**1.05**	–	1.00	1.90	−0.95	76.33	–
	T	3.22	2.07	2.61	78.02	20.53	8.01 (11.43)	M	–	1.00	1.96	−0.98	58.07	–
ScS_2	H	3.70	2.52	2.69	64.42	16.31	3.54 (6.71)	**0.44**	–	1.00	1.64	−0.82	44.41	–
	T	3.62	2.50	3.44	87.05	16.48	3.71 (6.88)	M	–	NM	1.62	−0.81	29.39	–
$ScSe_2$	H	3.84	2.65	2.90	66.39	15.12	3.23 (6.30)	**0.27**	–	1.00	1.56	−0.78	39.09	–
	T	3.52	2.64	3.94	96.42	15.42	3.54 (6.60)	M	–	NM	1.44	−0.72	**18.67**	–
$ScTe_2$	H	3.62	2.89	3.98	87.17	13.67	2.25 (5.39)	M	–	NM	1.34	−0.67	**38.28**	–
	T	3.72	2.85	4.33	98.58	14.05	2.63 (5.77)	M	–	NM	1.33	−0.67	**13.89**	–
TiS_2	T	3.32	2.39	3.42	91.73	18.36	3.97 (7.81)	M	–	NM	1.60	−0.80	76.33	1T[82]
$TiSe_2$	T	3.43	2.51	3.68	94.04	16.92	3.42 (7.15)	M	–	NM	1.39	−0.70	63.92	1T[83]
$TiTe_2$	H	3.62	2.75	3.57	81.09	14.76	1.72 (5.53)	M	–	NM	1.16	−0.58	**9.10**	1T[84]
	T	3.64	2.73	4.06	96.30	15.10	2.06 (5.87)	M	–	NM	1.18	−0.59	41.01	
VO_2	H	2.70	1.92	2.24	71.34	21.64	7.20 (11.13)	M	–	0.52	1.79	−0.90	171.98	*P*4/*ncc*,[85] *I*4/*m*[85]
VS_2	T	3.10	2.31	3.43	95.94	17.46	2.78 (6.45)	M	–	0.33	1.29	−0.65	104.26	1T[86,87]
	H	3.09	2.31	2.95	79.14	17.47	2.79 (6.46)	M	–	0.19	1.18	−0.59	106.03	
VSe_2	H	3.24	2.45	3.17	80.49	15.97	2.17 (5.74)	M	–	0.68	1.05	−0.53	82.90	1T[88]
	T	3.24	2.44	3.66	97.04	15.99	2.20 (5.76)	M	–	0.35	1.08	−0.54	80.16	
VTe_2	H	3.48	2.66	3.48	81.90	14.17	0.83 (4.48)	M	–	0.83	0.80	−0.40	49.66	1T[89]
	T	3.46	2.64	4.00	98.35	14.24	0.90 (4.55)	M	–	NM	0.83	−0.41	54.45	
CrO_2	H	2.58	1.88	2.29	75.21	19.55	6.25 (10.25)	**0.50**	**1.80**	NM	1.54	−0.77	220.94	R[90]
CrS_2	H	2.97	2.25	2.92	80.86	15.89	2.35 (6.09)	1.07	1.84	NM	0.92	−0.46	129.00	1T*[91]
$CrSe_2$	H	3.13	2.38	3.11	81.54	14.32	1.65 (5.30)	0.86	1.51	NM	0.77	−0.38	104.58	1T*[91]
$CrTe_2$	H	3.39	2.58	3.38	81.56	12.52	0.32 (4.04)	0.60	1.12	NM	0.46	−0.23	77.37	–
MnO_2	H	2.61	1.87	2.22	72.70	17.71	4.57 (9.59)	M	–	0.69	1.31	−0.65	134.07	R[92]
	T	2.82	1.88	2.50	83.07	18.43	5.28 (10.31)	0.28	–	3.00	1.64	−0.82	157.12	
MnS_2	T	3.12	2.27	3.29	93.08	14.82	1.43 (6.20)	M	–	2.38	0.92	−0.46	66.87	P[93−95]
$MnSe_2$	T	3.27	2.39	3.50	93.78	13.61	1.11 (5.77)	M	–	2.35	0.74	−0.37	56.61	P[96,97]
$MnTe_2$	T	3.54	2.59	3.77	93.56	12.27	0.22 (4.97)	M	–	2.29	0.41	−0.20	44.77	P[98,96]
FeO_2	H	2.62	1.88	2.24	73.08	17.37	3.25 (7.89)	M	–	1.82	1.38	−0.69	131.99	M[4]
FeS_2	H	3.06	2.22	2.68	74.20	15.50	1.14 (5.52)	M	–	1.12	0.57	−0.29	59.20	P,[19−23] Ma[6]
$FeSe_2$	H	3.22	2.35	2.87	75.36	14.93	1.45 (5.73)	M	–	1.18	0.42	−0.21	49.89	P,[99] Ma[100]
$FeTe_2$	H	3.48	2.53	3.08	74.98	13.21	0.19 (4.55)	M	–	1.08	0.06	−0.03	37.71	Ma[101]
$CoTe_2$	H	3.52	2.51	2.96	72.16	13.44	0.29 (4.67)	M	–	NM	−0.19	0.10	56.15	Ma[6,102]
NiO_2	T	2.77	1.84	2.44	82.82	16.76	3.10 (7.12)	**1.38**	–	NM	1.34	−0.67	146.64	1T[103]
NiS_2	H	3.40	2.24	2.14	57.16	14.35	0.45 (4.21)	M	–	NM	0.42	−0.21	39.51	P[104]
	T	3.28	2.12	2.97	84.46	14.91	1.00 (4.77)	**0.51**	–	NM	0.49	−0.24	86.23	
$NiSe_2$	H	3.33	2.35	2.71	70.29	13.49	0.47 (4.13)	M	–	NM	0.25	−0.12	35.92	P[104]
	T	3.46	2.34	3.15	84.59	13.97	0.95 (4.61)	**0.10**	–	NM	0.27	−0.13	62.73	
$NiTe_2$	H	3.59	2.54	2.93	70.55	12.92	0.36 (4.10)	M	–	NM	−0.12	0.06	41.00	1T[6]
	T	3.64	2.52	3.47	87.33	13.19	0.63 (4.37)	M	–	NM	−0.12	0.06	43.65	
NbS_2	T	3.30	2.45	3.62	95.25	19.64	3.17 (6.37)	M	–	NM	1.52	−0.76	96.60	1T,[105] 2H[106]
$NbSe_2$	T	3.39	2.57	3.87	97.48	18.13	2.56 (5.64)	M	–	NM	1.27	−0.64	70.47	2H,[107] 4H,[108]
	H	3.40	2.57	3.33	80.68	18.23	2.65 (5.74)	M	–	NM	1.23	−0.62	87.24	1T[6]
$NbTe_2$	T	3.56	2.77	4.24	100.05	16.38	1.26 (4.43)	M	–	NM	0.90	−0.45	64.08	1T[+109]
MoO_2	H	2.78	2.00	2.42	73.92	22.65	6.79 (10.63)	**0.97**	**2.42**	NM	1.84	−0.92	223.93	R[+],[110,111] Mcl[110,111]

dx.doi.org/10.1021/jp212558p | J. Phys. Chem. C 2012, 116, 8983−8999

Table 1. continued

	type	a (Å)	d_{M-X} (Å)	d_{X-X} (Å)	θ (deg)	E_C (eV)	E_f (eV)	E_g (eV)	$E_g^{GW_0}$ (eV)	μ (μ_B)	ρ_M (electrons)	ρ_X (electrons)	C (N/m)	3D bulk structure[h]
MoS_2	H	3.11	2.37	3.11	81.62	19.05	2.49 (6.53)	1.87	2.57	NM	1.04	−0.52	138.12	1T,[112,113] 2H,[112,113] 3R[112]
$MoSe_2$	H	3.24	2.50	3.32	83.05	17.47	2.25 (5.73)	**1.62**	**2.31**	NM	0.76	−0.38	118.37	2H,[114] 3R[115]
$MoTe_2$	H	3.46	2.69	3.59	83.88	15.65	0.89 (4.45)	1.25	**1.85**	NM	0.34	−0.17	92.78	2H,[6] 1T′[+6]
WO_2	H	2.80	2.03	2.45	74.12	24.56	6.72 (10.46)	**1.37**	**2.87**	NM	1.99	−1.00	250.00	R[+116]
WS_2	H	3.13	2.39	3.13	81.74	20.81	2.72 (6.21)	1.98	**2.84**	NM	1.22	−0.61	151.48	1T′,[+117] 2H[118]
WSe_2	H	3.25	2.51	3.34	83.24	19.07	1.86 (5.25)	**1.68**	**2.38**	NM	0.90	−0.45	130.04	2H[119]
WTe_2	H	3.47	2.70	3.61	83.96	17.05	0.30 (3.77)	1.24	**1.85**	NM	0.41	−0.20	99.17	1T′[+120]

[a]Values in parentheses were calculated using experimental cohesive energies of constituent elements. [b]Only for selected compounds. [c]Positive sign indicates depletion of electrons. [d]Negative sign indicates excess electrons. [e]Structures having indirect band gap according to LDA (and GW_0) calculations are indicated with bold face. [f]Abbreviations used for 3D bulk structures: 4H = 4H-MX_2, 2H = 2H-MX_2, 3R = 3R-MX_2, 1T = 1T-MX_2 structure; R = rutile, P = pyrite, M = molecule, Mcl = monoclinic, Ma = marcasite crystal structure. [g]All values in this table were calculated using LDA, as detailed in the Method section. [h]Metastable crystal, *; distorted lattice structure, +.

values. In our study, the LDA and GGA + vdW predictions were 3.11 and 3.22 Å, respectively.

In closing this section, we point out that the energetics discussed here, namely, the cohesive energies or formation energies of the MX_2 single-layer H and T structures, do not change significantly in their layered 3D crystals. Even if some dimensionality effects can be observed,[46,47] the interactions between adjacent layers are usually weak and on the order of 100−200 meV. Earlier studies showed[41−43] that the interlayer interactions originate mainly from van der Waals attractions, and hence, stacking or surface energy of 3D MX_2 crystals is expected to be small and in the range of ∼100 meV.

Lattice Dynamics. Even if the total energy of a structure can be minimized, its stability cannot be assured. Therefore, frequencies of the vibration modes of optimized single-layer MX_2 in the H or T structure were calculated for all $\mathbf{k}$ points in the BZ to provide a rigorous test for the stability of a given structure. A structure is taken to be stable only when calculated frequencies of all phonon modes in the BZ are positive; otherwise, imaginary frequencies indicate instability. In such calculations, the long-wavelength, out-of-plane acoustical (ZA) modes are vulnerable to instability. Thus, caution has to be taken in calculating forces with extreme accuracy.[121]

In Figures 4 and 5, we present the calculated phonon branches of MX_2 compounds in the H and T structures, respectively, which display three acoustical branches separated by a gap from six optical branches. All 52 2D single-layer MX_2 compounds presented in Figures 4 and 5 have positive frequencies in the BZ, except for a few of them that have imaginary frequencies in a small region of $\Omega(k) \to 0$ (or $\lambda \to \infty$). Calculations of frequencies in this region of the BZ require very high accuracy for the calculation of forces. Therefore, the structural instability as $\lambda \to \infty$ might arise due to numerical calculations. Even if the instability of MX_2 compounds as $\lambda \to \infty$ were a reality, the compounds could be stabilized at small sizes. Moreover, because of limitations of DFT for highly correlated electron systems, some MO_2 compounds having H and T structures can have imaginary frequencies at the center of the BZ. Nonetheless, in the following sections, we further explore the possible instabilities of specific compounds using finite-temperature ab initio MD and LDA + U calculations.

The phonon frequencies of the series of MoX_2 (X = O, S, Se, and Te) are plotted on the same scale of frequency in Figure 6 for the sake of detailed discussion of the trends related to chalcogen atoms. As the row number of X decreases, the X atoms become lighter, and the M−X bonds become more ionic. Consequently, the width of the acoustical branches increase from Ω = 119 cm^{-1} to Ω = 405 cm^{-1}, and the highest frequency of the optical modes also increases as X goes from Te to O. As an example, whereas the highest frequency of the transverse optical (TO) mode of $MoTe_2$ at the Γ point is Ω = 298 cm^{-1}, the frequency of the same mode of MoO_2 occurs at Ω = 733 cm^{-1}. Among stable single-layer MX_2 compounds, CrO_2 has the highest TO frequency, $\Omega(k = 0)$ = 824 cm^{-1}. That the width of the phonon branches increases with decreasing row number of X atoms generally occurs for other M atoms in both the H and T structures. Longitudinal acoustic (LA) branches have linear dispersions as $\mathbf{k} \to 0$, whereas ZA (out-of-plane) modes display parabolic dispersion owing to the rapid decay of transverse force constants.

Owing to the limited experimental data on the phonon spectrum, we checked our results regarding the lattice dynamics of stable H and T structures of MX_2 crystals with the available Raman (R) and infrared (IR) data. Because experimental data are available only for single-layer MoS_2 and WS_2, one can compare the frequencies of Raman-active modes calculated for these single-layer compounds. The calculated frequencies of the Raman-active modes, namely, E′ = 380 cm^{-1} and A′$_1$ = 406 cm^{-1}, are in agreement with the corresponding experimental data,[46] E′ = 384 cm^{-1} and A′$_1$ = 403 cm^{-1}. Similarly, the LDA-calculated frequencies of Raman-active modes of WS_2, E′ = 359 cm^{-1} and A′$_1$ = 412, are in fair agreement with the experimental data,[47] E′ = 350 cm^{-1} and A′$_1$ = 415 cm^{-1}. Also, experimentally, the IR-active modes at the center of the BZ are observed as 384 and 470 cm^{-1}, which were predicted in the present study using LDA as 359 and 437 cm^{-1}, respectively. Moreover, the Raman-active modes calculated by LDA are able to reproduce the anomalous dimensionality effect between 3D 2H-MoS_2 and 2D MoS_2 in the H structure as revealed by Lee et al.,[46] namely, that whereas the A′ mode softens, E′ becomes stiffer upon going from 2D to 3D.

Significant charge transfer and resulting polar character is the marked feature of 2D MX_2 compounds. Unlike graphene and silicene,[30,57−61,122,123] the H and T structures of MX_2 exhibit an interesting charge distribution, as shown in Figures 1 and 2, specifically, the outer planes of X atoms are negatively charged, whereas the plane of M atoms between them is positively charged. Bader analysis[73] indicates that electrons from M atoms

dx.doi.org/10.1021/jp212558p | J. Phys. Chem. C 2012, 116, 8983−8999

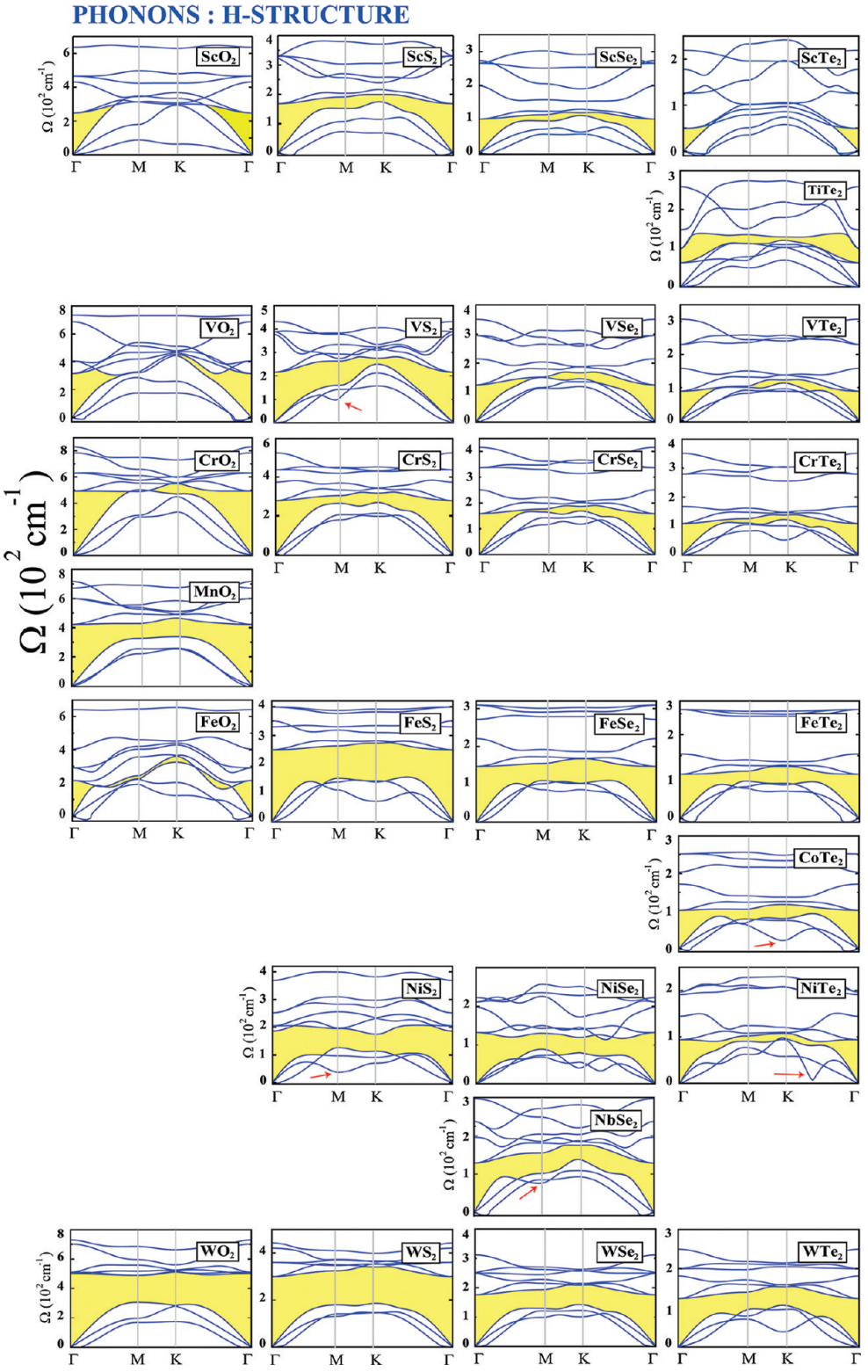

Figure 4. Calculated phonon branches of 2D single-layer MX_2 compounds that are stable in the H structure. Phonon dispersions are presented along the Γ−*M*−*K*−Γ directions of the BZ. The gaps between acoustical and optical branches are shaded. The transverse acoustical ZA branch has parabolic dispersion as $\mathbf{k} \rightarrow 0$. Different scales of frequency are used for different materials. The phonon dispersion curves of MoX_2 (X = O, S, Se, and Te) are presented in the same scale of frequency in Figure 6. Dips that can be associated with Kohn anomalies are indicated by arrows.

are transferred to two X atoms, leaving a depletion of electronic charge on M (i.e., $\rho_M > 0$) and an excess of electronic charge on X (i.e., $\rho_X < 0$). As expected, $\rho_M = 2|\rho_X|$. However, $CoTe_2$ and $NiTe_2$ appear to be exceptions, where the direction of charge transfer is reversed according to Bader analysis. Also, excluding a few exceptions in transition-metal oxides, ρ_M increases with decreasing row number of the X atom. The Born effective charges, which can be obtained from the treatment of lattice

dx.doi.org/10.1021/jp212558p | J. Phys. Chem. C 2012, 116, 8983−8999

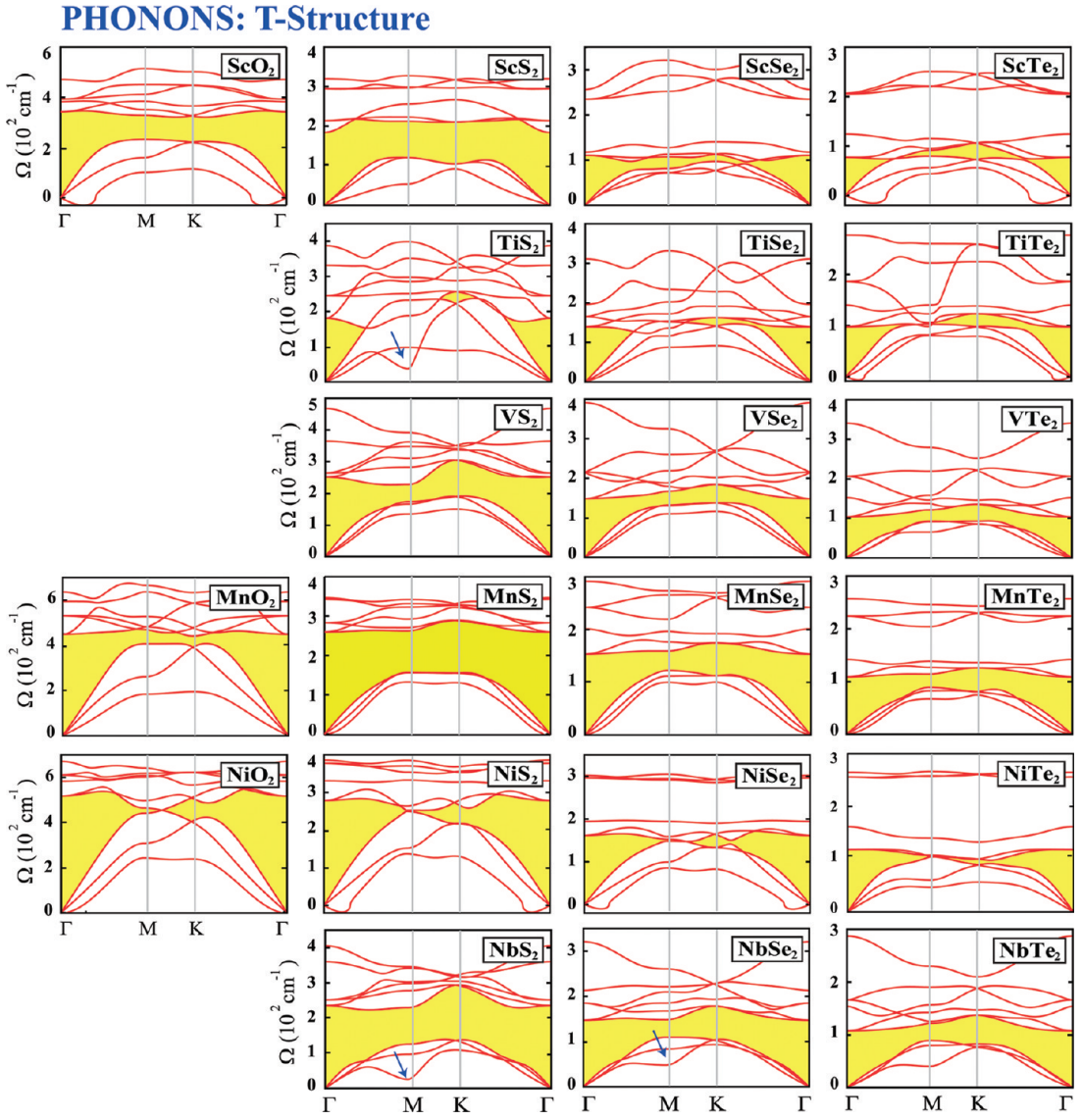

Figure 5. Calculated phonon branches of 2D single-layer MX_2 compounds that are stable in the T structure. Phonon dispersions are presented along the $\Gamma-M-K-\Gamma$ directions of the BZ. The gaps between acoustical and optical branches are shaded. The transverse acoustical ZA branch has parabolic dispersion as $\mathbf{k} \rightarrow 0$. Different scales of frequency are used for different materials. Dips that can be associated with Kohn anomalies are indicated by arrows.

dynamics, are in compliance with the direction of charge transfer revealed through the Bader analysis of MoS_2. For example, the Born effective charges calculated for MoS_2 are $Z^{\parallel}_{Mo} = 1.211$, $Z^{\perp}_{Mo} = 0.075$ electron and $Z^{\parallel}_{S} = -0.573$, $Z^{\perp}_{S} = -0.043$ electron.

The phonon dispersion curves of specific compounds, such as VS_2, $CoTe_2$, NiS_2, $NiTe_2$, and $NbSe_2$ in the H structure and TiS_2, NbS_2, and $NbSe_2$ in the T structure, exhibit dips or local minima in the BZ, as seen in Figures 4 and 5. Even more remarkable is that an acoustical branch of $NiTe_2$ dips until its frequency becomes zero for $\mathbf{k}$ between K and Γ points. These structures in the phonon bands lead to discontinuities in $\partial\Omega/\partial k$ and are associated with Kohn anomalies.[124] They occur at specific $\mathbf{k}$ vectors in the BZ, where the dielectric constant $\varepsilon(k)$ goes through a singularity, causing an abrupt change in the electron screening of the lattice potential. This singularity, in turn, is reflected in the phonon dispersion curves. $NiTe_2$ is an extreme case, which can happen in low-dimensional materials and indicates a static distortion of the crystal.

Ab Initio Molecular Dynamics Calculations. If the analysis based on phonon calculations indicates the stability of an MX_2 compound under study at $T = 0$ K, this stability could be destroyed at elevated temperatures. In certain cases, the stable structure might correspond to a shallow minimum in the Born−Oppenheimer surface, in which case the instability occurs already at low temperatures. Additionally, in certain structures, imaginary frequencies for phonon modes can occur near the center of the BZ. Thus, one has to clarify whether imaginary frequencies occurring for $\lambda \rightarrow \infty$ can cause an instability or whether they are only an artifact of numerical calculations. If a structure is unstable at $T = 0$ K, it is distorted or disintegrated when atoms are displaced from their equilibrium positions in the course of a large number of time steps between two velocity normalizations. Thus, the possibilities that a compound can be unstable were further tested for specific compounds using first-principles molecular dynamics (MD) calculations at temperatures of $T = 500$, 1000, and 1500 K. The time steps were taken to be 2×10^{-15} s, and

dx.doi.org/10.1021/jp212558p | J. Phys. Chem. C 2012, 116, 8983−8999

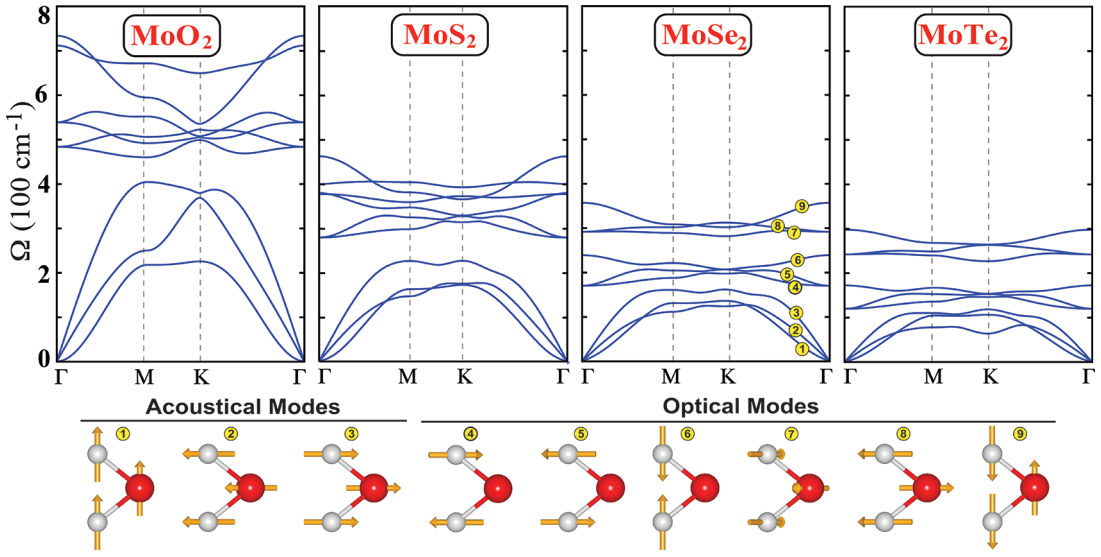

Figure 6. Calculated phonon branches of stable H structures of MoX_2 (X = O, S, Se, and Te) compounds along the Γ–*M*–*K*–Γ directions of the BZ. Phonon branches are labeled by numerals. The acoustical and optical phonon modes at the Γ point are depicted in the bottom panel. All branches are presented using the same scale of frequency.

the velocities of the atoms were normalized every 40 steps for T = 500 K and every 100 steps for T = 1000 and 1500 K.

For the H structure, we considered $FeTe_2$, MoO_2, VO_2, and VSe_2. The first three compounds have 3D crystals that are different from layered 2H and 1T structures, and hence, it seems unlikely that these three compounds can occur in stable H structures. In addition, because of the imaginary frequencies as $\Omega(\mathbf{k}) \rightarrow 0$ in a small region, $FeTe_2$ and VO_2 are vulnerable to instability as $\lambda \rightarrow \infty$. VSe_2 has a layered 1T structure, and hence, one needs to confirm whether the H structure can really occur even if it is less energetic than the T structure. To avoid the stability, which can be imposed by periodic boundary conditions using a (1×1) unit cell, calculations were carried out using (4×4) supercells. All four compounds remained intact after many steps (300 time steps) at T = 500 K. If they were unstable already at T = 0 K, their structure would be dissociated at this temperature even before 300 time steps. Then, calculations were switched to T = 1000 K starting from atomic velocities of the final step at T = 500 K. Higher temperatures and normalization at relatively larger numbers of steps can speed the onset of the instability, which would normally occur at relatively lower temperatures after a large number of steps. If the system continues to remained stable after a sufficiently large number of steps at T = 1000 K, we raised the temperature and let the MD calculations run at T = 1500 K. The temperature T = 1500 K is rather high and is expected to accelerate the occurrence of a structural instability, which could have occurred at relatively low temperatures. In fact, whereas the H structure of $FeTe_2$ remained stable after 304 steps at T = 1000 K, it severely distorted after 562 steps at T = 1500 K. MoO_2 in the H structure was stable after 546 steps at T = 1000 K and remained stable after 760 steps at T = 1500 K. We concluded that MoO_2 can remain stable in the H structure at moderate temperatures. The situation with VO_2 is similar to that of MoO_2, except that an O atom desorbed after 530 time steps at T = 1500 K. VSe_2 continued to be stable after 1429 time steps at T = 1500 K. The final geometries of MX_2 structures after several time steps are shown in Figure 7.

For the T structure, we considered MnS_2, $ScTe_2$, and $NiSe_2$, because their specific acoustical modes have imaginary frequencies near the center of the BZ. Ab initio MD calculations showed that MnS_2 was stable after 740 steps at T = 1000 K and continued to be stable after 700 steps at T = 1500 K with almost-perfect centered honeycombs. However, the situation was different for $ScTe_2$ and $NiSe_2$. $ScTe_2$ became distorted already after 1281 time steps at T = 1000 K and became severely distorted and dissociated after 1041 time steps at T = 1500 K. The centered honeycomb structure of $NiSe_2$, which was maintained after 200 steps at T = 1000 K, was severely distorted after 652 time steps at T = 1500 K. These results of MD calculations imply that imaginary frequencies near the center of the BZ revealed from the phonon calculations of $ScTe_2$ and $NiSe_2$ having T structures are not artifacts of numerical accuracy.

In concluding this section, the present analysis shows that single-layer MX_2 compounds having positive frequencies at all $\mathbf{k}$ points in the BZ are stable at 0 K; most of them continue to be stable above room temperature, once they are synthesized or produced in the H or T structures. On the other hand, specific compounds for which imaginary frequencies are calculated near the center of the BZ can be vulnerable to structural instability, if these frequencies are not artifacts of numerical accuracy and these compounds are not stabilized because of their small size. Similarly, relatively small formation energies E_f and/or small in-plane stiffness values C (presented in Table 1) calculated for any single-layer MX_2 compound can also imply the instability. Under these circumstances, ab initio MD calculations present evidence that a compound is unstable and ready for dissociation. In this respect, among compounds that needed further tests through ab initio MD calculations, the stabilities of $FeTe_2$ and VO_2 in the H structure and $ScTe_2$ and $NiSe_2$ in the T structure were found to be weak.

Mechanical Properties. The strength of nanostructures is crucial for their use in diverse nanotechnology applications. Elastic constants can provide further indications about the strength of stable H and T structures. A honeycomb structure usually underlies the unusual mechanical properties providing high in-plane strength and flexibility in deformations perpendicular to the atomic planes. We focused on the harmonic range of the elastic deformation, where the structure

dx.doi.org/10.1021/jp212558p | J. Phys. Chem. C 2012, 116, 8983–8999

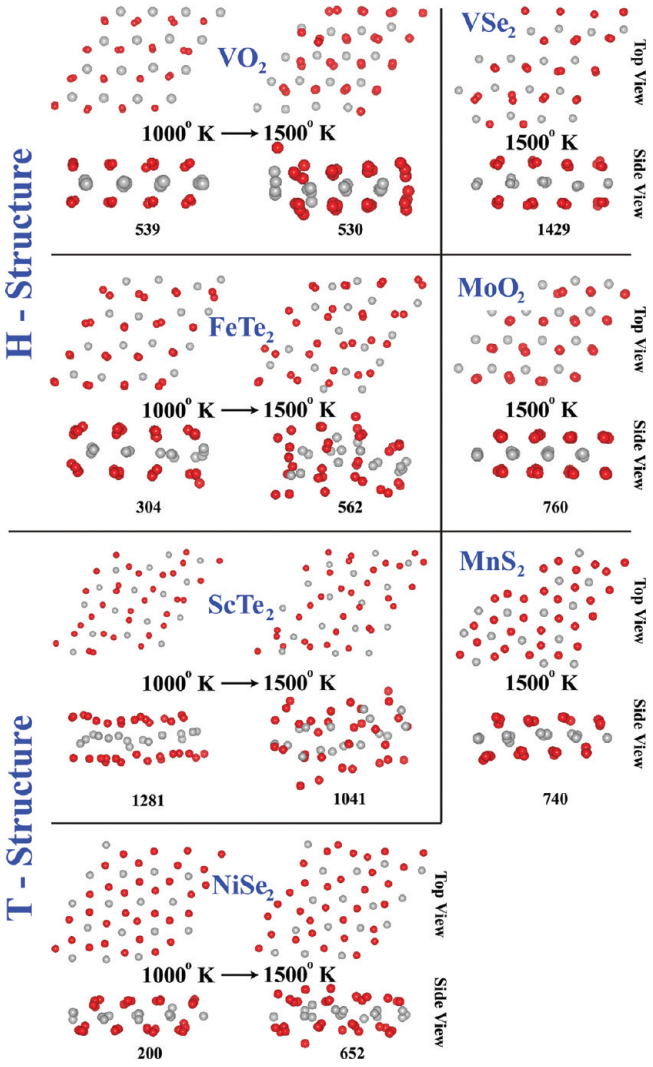

Figure 7. Top and side views of snapshots corresponding to atomic structures of selected MX_2 compounds taken from ab initio molecular dynamic (MD) calculations at specified temperatures and time steps indicated by numerals below each panel. MD results at T = 1000 K are also shown for structures that become unstable at T = 1500 K.

responded to strain ε linearly and reversibly. Here, ε is the elongation per unit length. The strain energy is defined as $E_S = E_T(\varepsilon) - E_T(\varepsilon = 0)$, that is, the total energy at a given strain minus the total energy at zero strain. Normally, the Young's modulus characterizes the mechanical strength of bulk materials. However, the definition of the width of an H or T structure is not unambiguous, and hence, instead of the Young's modulus of a single-layer MX_2 structure, one can use the in-plane stiffness $C = (1/A_0)(\partial^2 E_S/\partial\varepsilon^2)$, in terms of the uniform stress and equilibrium area of the supercell, A_0.[31] The calculated in-plane stiffness values of single-layer MX_2 materials presented in Table 1, ranging from 250 to 9 N/m, can be contrasted with the values calculated for graphene and BN, 357 N/m (experimental value 340 ± 50 N/m) and 267 N/m, respectively. We note that, generally, in-plane stiffness values increase with decreasing row number of X; stated differently, an MX_2 compound softens as the row number of X increases. Thus, the calculated values of C are usually low for compounds having X = Te. This trend is in compliance with the trend outlined in Figure 6. The in-plane stiffness of WX_2 is usually higher than those of other MX_2 compounds. Also, the C value of the H structure is usually higher than that of the T structure if both structures occur for the same compound. Finally, MX_2 compounds having C values that are marked by boldface in Table 1 do not deform symmetrically. A low value of C and nonuniform deformation under uniform stress imply possible instability at finite temperatures.

■ ELECTRONIC AND MAGNETIC PROPERTIES

The stable MX_2 compounds in the H and T structures display a rich diversity of electronic and magnetic properties. Depending on the combination of M and X, single-layer MX_2 compounds can be semiconductor, ferromagnetic, or nonmagnetic metals. In Figures 8−10 we present the electronic energy band structures of all stable MX_2 compounds having H and T structures. Because of the available experimental data, the band structure of the manifold MoX_2 (X = O, S, Se, Te) in the H structure is given separately in Figure 10 for detailed discussion. The MS_2 manifold (M = Sc, V, Cr, Fe, Ni, and W) includes semiconductors and magnetic and nonmagnetic metals in both the H and T structures.

Semiconducting single-layer MX_2 compounds having the H structure can be treated in two groups that display rather different band structures. The first group, transition-metal oxides (i.e., M = Sc, Cr, Mo, W; X = O) differ from the other group (i.e., M = Cr, Mo, W; X = S, Se, Te) by their relatively smaller band gaps and lower band-edge state densities. Here, we discuss these groups by considering the band structures of MoO_2 and MoS_2 as prototypes, as shown in Figure 10. For both groups, the bands at the edges of the conduction and valence bands are composed from Mo 4d and X p orbitals. However, the types (symmetries) and contributions of these orbitals vary with **k** and with the constituents M and X. The M−X bonds of single-layer MoO_2 are 0.3−0.7 Å shorter than those of the second group. As a result, the highest valence band at Γ, which is combined from Mo d_{z^2} and O p_z orbitals has higher dispersion. This band is pushed up toward the conduction band to lower the indirect band gap between the conduction-band minimum at the K point and the valence-band maximum at the Γ point. Accordingly, the smallest band gaps of all MO_2 honeycomb structures including MoO_2 are indirect. On the other hand, the topmost valence band of MoS_2, which has a relatively higher Mo d_{z^2} contribution and relatively longer M−X bonds, is flattened, and its energy is lowered. Under these circumstances, the smallest band gap of the second group is usually direct (except for $MoSe_2$, which has an indirect gap only 4 meV smaller than the direct one) and occurs at the K point between the conduction-band minimum (80% Mo d and 20% S p_x) and the valence-band maximum (90% Mo $d_{x^2-y^2}$ and 10% S p_x). The characters of these states at the K point are similar for X = S, Se, and Te, but their direct band gap decreases slightly on going from S to Te, because the lattice constants, $a = b$, increase from 3.12 to 3.46 Å. The isosurface charge densities of states at the band edges of $MoSe_2$ and $MoTe_2$ are also presented. The direct band gap of MoO_2 at the K point is significantly larger than that of MoS_2, because the Mo−O bond is much shorter (2.78 Å). The distinction between the energy band structures of the first group and the second group is also seen in the calculated total and orbital densities of states given in Figure 10. Another noteworthy trend that we deduced from our calculations is that, for all single-layer MX_2 semiconductors, the band gap generally increases as M goes from Sc to W. Despite the striking similarity of the band structures of MX_2

dx.doi.org/10.1021/jp212558p | J. Phys. Chem. C 2012, 116, 8983−8999

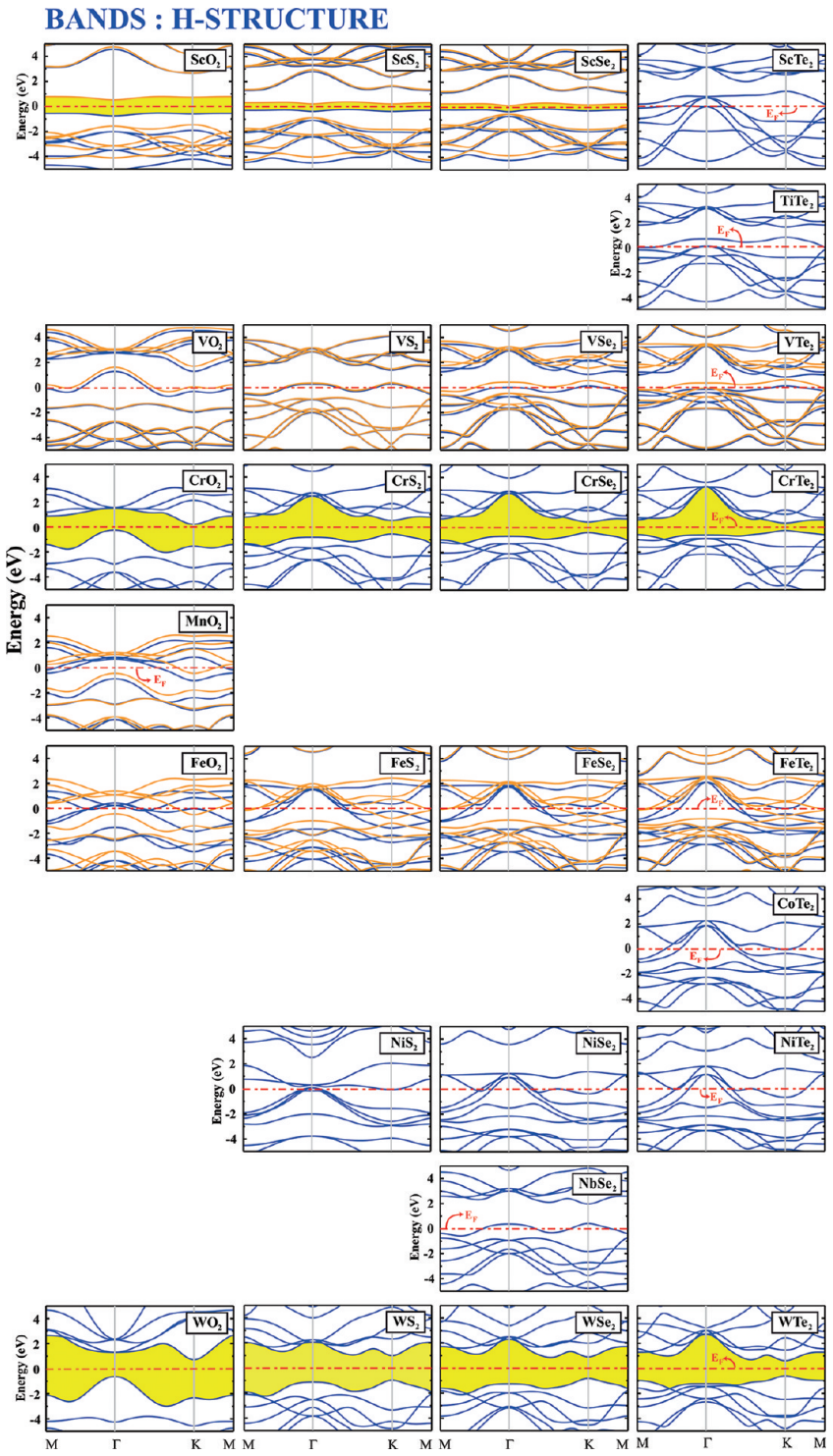

Figure 8. Calculated electronic band structures of 2D stable MX_2 compounds that are stable in the H structure. The zero of the energy is set to the Fermi level, E_F, shown by red dash-dotted lines. The energy gaps of semiconductors are shaded (yellow). For nonmagnetic states, spin-degenerate bands are shown as blue lines. For magnetic structures, blue lines represent spin-up bands, whereas orange lines are spin-down states. In the same row, stable structures with the same M atom but different X atoms are presented. Columns present the MX_2 manifold with the same X atom but differing M atoms. The manifold MoX_2 (X = O, S, Se, Te) in the H structure is presented separately in Figure 10.

(X = O, S, Se, and Te) as M goes from V to W, they are essentially either metal or semiconductor depending on the number of s and d valence states of the free M atoms.

We note that ferromagnetic metals, such as VX_2 or FeX_2 (X = O, S, Se, Te), in the H structure have magnetic moments that are located at the d orbitals of the transition-metal atoms. However, in the case of ScX_2 (X = O, S, Se), the magnetic moment is located at the site of the chalcogen atoms because of the crucial amount of transfer of charge from Sc to X, since Sc atom have relatively low electronegativity with respect to that of chalcogen atoms. In all magnetic structures, we further carried out supercell calculations to take into account the

dx.doi.org/10.1021/jp212558p | J. Phys. Chem. C 2012, 116, 8983–8999

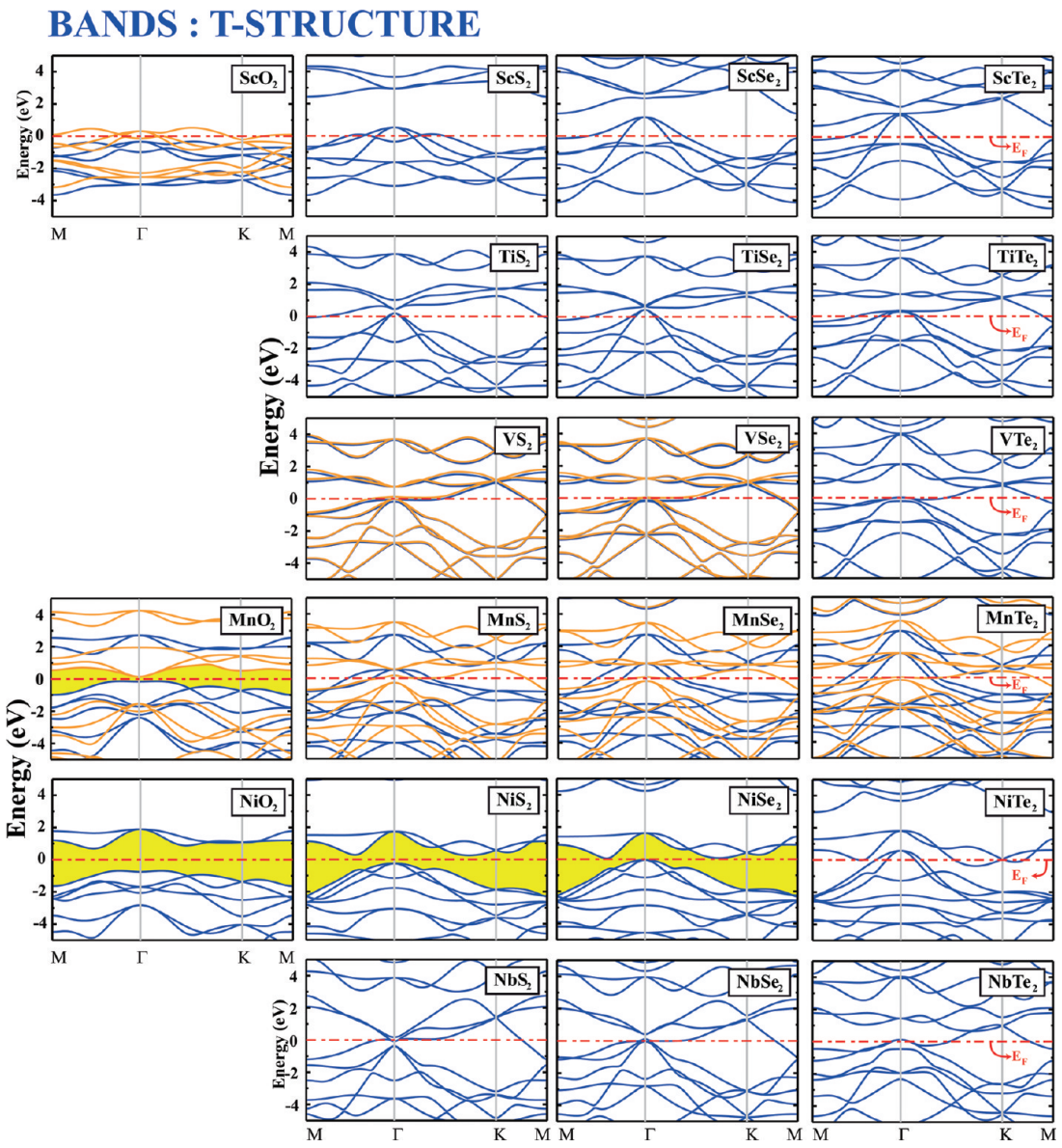

Figure 9. Calculated electronic band structures of 2D stable MX_2 compounds that are stable in the T structure. The zero of the energy is set to the Fermi level, E_F, shown by red dash-dotted lines. The energy gaps of semiconductors are shaded (yellow). For nonmagnetic states, spin-degenerate bands are shown as blue lines. For magnetic structures, blue lines represent spin-up bands, whereas orange lines are spin-down states. The manifold MX_2 with the same M atom but different X atoms is presented in the same row. Columns present MX_2 manifolds with the same X atom but differing M atoms.

antiferromagnetic ordering in neighboring unit cells. We conclude that ferromagnetic ordering is the energetically most favorable arrangement. We also addressed the question of whether the metallicity of MO_2 compounds, namely, VO_2, MnO_2, and FeO_2, in the H structure and ScO_2 in the T structure, is an artifact of LDA. Normally, these oxides are expected to be wide band gap semiconductor. To this end, we carried out electronic energy structure calculations using HSE06[74,75] functionals, which confirmed our LDA results.

Because DFT usually underestimates band gaps, we first compared the band gap calculated for 3D layered 2H-MoS_2 with the corresponding experimental values. The present study estimates the indirect band gap of 2H-MoS_2 as 0.72 eV, which is 0.51 eV smaller than the experimental value of E_g = 1.23 eV.[125] It is well-known that the bulk band gaps of Si and Ge are also underestimated by LDA. Under these circumstances, the band gaps of 3D 2H-MoS_2 and 2D MoX_2 manifold in the H structures were corrected by carrying out frequency-dependent GW_0 calculations.[76] In these calculations, the screened Coulomb potential, W, is kept fixed to the initial DFT value W_0, and the Green's function, G, is iterated several times. Various tests regarding vacuum separation; kinetic energy cutoff; and numbers of bands, **k** points, and grid points were made. Final results of for the GW_0 corrections were obtained using (12 × 12 × 1) **k** points in the BZ, a 400-eV cutoff potential, 192 bands for single-layer structures (384 for 3D 2H-MoS_2), and 64 grid points. The GW_0-corrected band gap of 2H-MoS_2 was found to be 1.28 eV, which is in good agreement with experimental value of 1.23 eV.[125]

The band gap of single-layer 1H-MoS_2 was calculated as 1.87 eV with LDA, whereas a recent experimental study[34] using complementary techniques of optical absorption, photoluminescence,

dx.doi.org/10.1021/jp212558p | J. Phys. Chem. C 2012, 116, 8983−8999

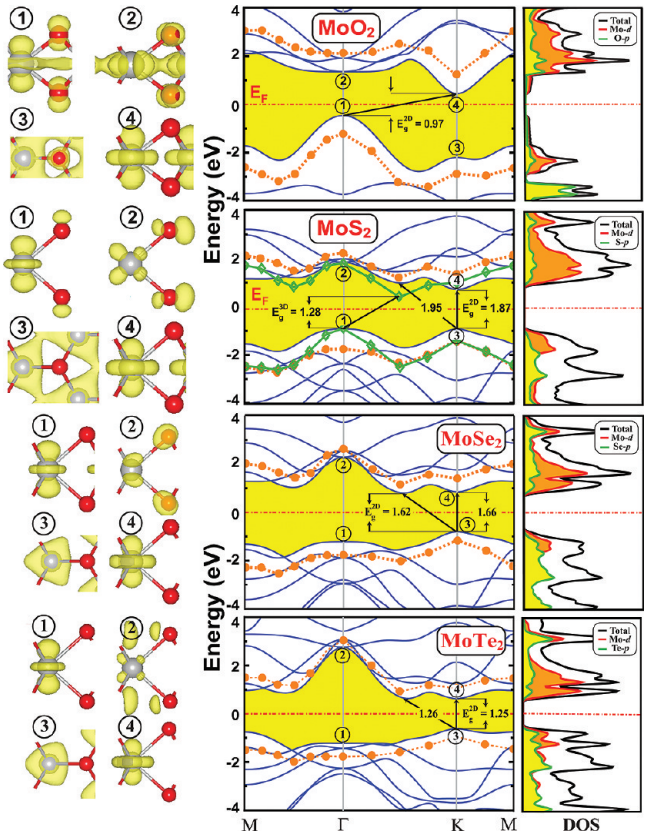

Figure 10. Calculated energy band structures, charge densities, and state densities of single-layer MoX_2 (X = O, S, Se, and Te). Left panels are isosurface charge densities of the specific states at the band edges indicated by numerals. The isosurface value is taken as 0.01 electron/Å^3. Middle panels are band structures along the $M-\Gamma-K-M$ directions of the Brillouin zone. The LDA band gap between the conduction and valence bands is shaded. The zero of energy is set at the Fermi level, E_F, shown by red dash-dotted line. The GW_0-corrected bands are indicated by orange dashed lines and dots. The GW_0-corrected band gap of 3D 2H-MoS_2 is indicated by green lines and diamonds. Direct and indirect band gap values are given in units of eV. Right panels are total and orbital-projected densities of states.

and photoconductivity reported its value as 1.90 eV. The band gap increased by ~0.70 eV and changed from indirect to direct upon going from a 3D layered stucture to the single-layer H structure. Three-dimensional 2H-MoS_2 consists of 1H-MoS_2 layers attracted by a weak van der Waals interaction of 96 meV per layer.[43] The chemical interaction is negligible (only 7 meV), and the interlayer spacing is large ~6.1 Å. Under these circumstances, it is remarkable that confinement effects can give rise to such a change in the band gap.[34] In Figure 10, the change from an indirect to a direct gap by lowering the dimensionality from 3D to 2D is shown. This transition of indirect to direct gap is expected to occur gradually as the number of layers in MoS_2 sheets decreases and could have important implications.[34,40]

Here, we address a crucial issue that the LDA result for 2D 1H-MoS_2 is so close to the experimental value, whereas it underestimates the 3D bulk value by 0.51 eV. On the other hand, the situation that the band gap of 2H-MoS_2 (which is underestimated by LDA as 0.72 eV) is successfully corrected by GW_0 as 1.28 eV, whereas the band gap of single-layer 1H-MoS_2 (which is predicted successfully by LDA as 1.87 eV) is overestimated upon GW_0 correction as 2.57 eV is rather paradoxical. Incidently, similar situations also occur for other single-layer honeycomb structures. For example, GW_0 corrections result in surprisingly large band gap values for single-layer BN and CF (fully fluorinated graphene) and graphane CH having honeycomb structures.[126] (The LDA band gap of fully fluorinated graphene CF is 2.98 eV, the LDA + *GW*o corrected band gap is 7.49 eV, and the experimental band gap is 3.0 eV.[127] Also, for graphane CH, the LDA band gap is 3.42 eV, and the LDA + GW_0 correction is 5.97 eV.[128]] Not only LDA + GW_0 but also the screened-nonlocal-exchange HSE[74] functional recommended for localized d bands yielded band gap of MoS_2 significantly larger than 1.90 eV with/without the GW_0[42,75] correction. These results suggest that the overestimation of the band gap of some single-layer structures by the GW_0 correction might originate from the fact that LDA alone already provides a good estimate of the band gap of 1H-MoS_2. It is expected that the same situation might be valid for other MX_2 semiconductors and that their band gaps can be overestimated by the GW_0 correction. Unfortunately, we cannot further explore the capacity of the GW_0 correction for other single-layer H and T structures, because no experimental data exist for comparison. Nevertheless, this paradoxical situation will be resolved when additional experimental data on the band gaps of single-layer MX_2 structures become available. It is also emphasized that, whereas MO_2 compounds (for M = Cr, Mo, and W, which occupy the same column in the Periodic Table) are indirect-band-gap semiconductors, other MX_2 compounds with M = Cr, Mo, and W and X = S, Se, and Te are direct-band-gap semiconductors.

The bands of MX_2 in the T structure are given in Figure 9: Like MoX_2 manifolds in the H structure, nonmagnetic semiconductors occur in NiX_2 with X = O, S, and Se. $NiTe_2$ is nonmagnetic metal in the T structure. NiS_2, $NiSe_2$, and $NiTe_2$ can occur in both the T and H structures, with the T structure being 0.2−0.5 eV energetically more favorable. However, energy band structures display significant differences by going from the T to the H structure. Whereas NiS_2 and $NiSe_2$ are nonmagnetic metals in the H structure, the same compounds are narrow and indirect-band-gap semiconductors in the T structure. Even if 3D NbX_2 (X = S, Se, and Te) can occur in the 1T and 2H structures, NbS_2 and $NbTe_2$ are stable only in the T structure. Even if $NbSe_2$ can have both H and T structures, it is metallic in the H structure and 12 meV more energetic than the corresponding T structure. Two-dimensional and suspended $NbSe_2$ in the H structure is of particular interest, because 3D $NbSe_2$ is a superconductor. As for the NiX_2 manifold, VX_2 (X = S, Se, and Te) compounds form both T and H structures, which have practically same cohesive energies within the accuracy limits of the numerical calculations carried out in the present study. In Figure 11, we compare the total and orbital projected densities of states of these structures. Despite the small energy differences between the T and H structures of these compounds, significant differences and striking common features in electronic structures are revealed. For example, for VX_2 in the T and H structures, one recognizes differences in the densities of states. However, for both structures, the densities of states at E_F originate from V 3d states and are rather high. As for NiX_2, the character of the bands undergoes a change upon going from the T to the H structure.

LDA + *U* Calculations. It is known that electrons in transition-metal oxides are highly correlated, which, in turn, can limit the application of DFT to this class of materials. In this

dx.doi.org/10.1021/jp212558p | J. Phys. Chem. C 2012, 116, 8983−8999

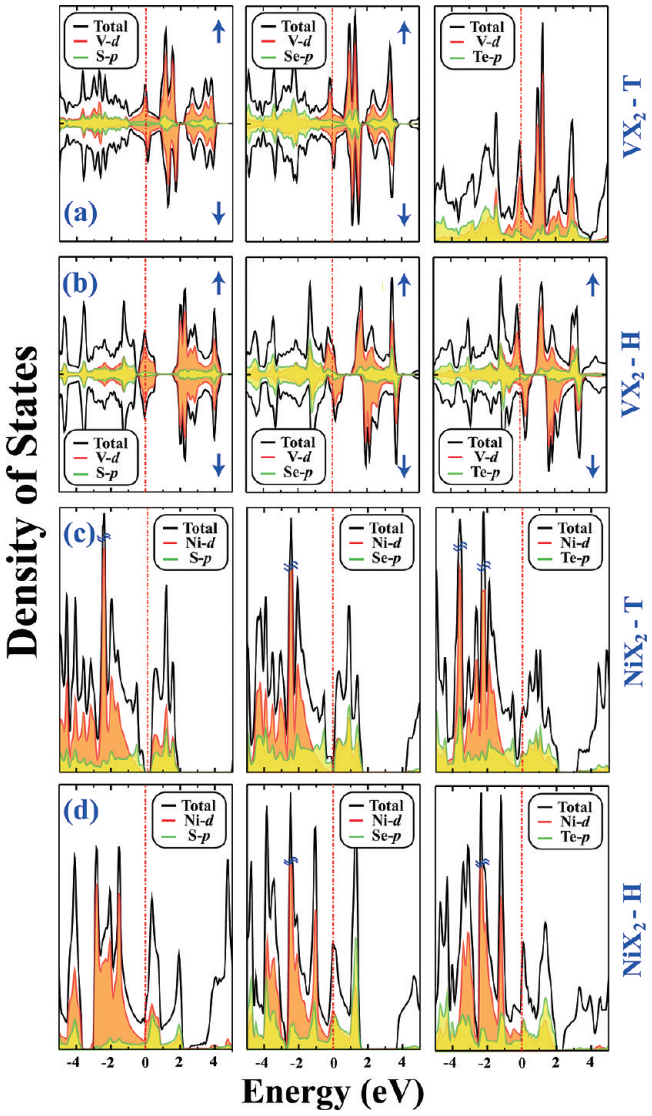

Figure 11. Comparison of the electronic structures of specific suspended MX_2 compounds forming both stable T and H structures. Total densities and orbital-projected densities of states of (a,b) 2D VS_2, VSe_2, and VTe_2 compounds and (c,d) 2D NiS_2, $NiSe_2$ and $NiTe_2$ compounds in (a,c) T and (b,d) H structures. The zero of the energy is set to the Fermi level, E_F, shown by red dash-dotted line. Up and down arrows indicate spin-up and spin-down densities of states. Total densities of states are given by thick solid lines.

respect, predictions obtained using DFT on the stabilities and band gaps of MO_2 compounds should be taken with caution. Surprisingly, in most cases, LDA provides reasonable predictions even for correlated systems. To model additional properties, one must take into account the double-counting terms. For this reason, all LDA + U functionals can be written as a difference of interaction terms and double-counting corrections. Even though there is a single interaction term, double-counting terms differ. Most commonly used ones for the double-counting terms are the fully localized limit (FLL) and around mean field (AMF).[129] The main difference between them is how they include U in the correction. The effect of U is dominant in AMF, so that it suppresses the magnetic state. For this reason, FFL is generally accepted to perform better for high-spin states, whereas AML is good for low-spin systems.

We carried out LDA + U corrections on NiO_2 and ScO_2 in the T structure and on WO_2 in the H structure using the method introduced by Dudarev et al.[71] Our calculations were performed using the FFL approximation. In this method, the total energy of the system depends on $U - J$ term, where U is the on-site Coulomb repulsion or Hubbard term and J is the exchange parameter. Because realistic values of U and J for compounds having either H or T structures are not yet available, we instead took $U - J$ as a parameter varying between 1 and 11 eV and examined its effects on the band gap and lattice constant, as well as on the stability of MO_2. Therefore, our analysis can provide only trends in how the band gaps and lattice constants of MO_2 in the H and T structures vary with $U - J$.

Bare LDA indicates that ScO_2 has a half-metallic ground state with integer magnetic moment per unit cell. Spin-up bands have a gap between filled and unoccupied bands, whereas three spin-down bands derived from oxygen p orbitals cross the Fermi level and hence are metallic. The isosurfaces of the difference charge densities of spin-up and spin-down states suggest that the magnetic moment arises from the excess charge on O transferred from Sc atoms. Accordingly, the Hubbard U correction is taken into account for both 3d orbitals of transition-metal atom and 2p orbitals of O. Upon LDA + U calculations, two of the three metallic bands are not affected, but the energy of the third band derived from the O p_z orbital increases with increasing U energy. Eventually, the metallic spin-down bands split and open a band gap to become also semiconductor when $(U - J) > 4$. In addition, the size of the unit cell by up to 6% for $(U - J) = 11$ eV.

Bare LDA predicts that both NiO_2 and WO_2 are nonmagnetic semiconductors. The band at the edge of valence band of NiO_2, which is nondispersive around the Γ point, is derived mainly from 3d orbitals, whereas bands slightly below the valence band edge are derived from O 2p orbitals. In LDA + U calculations, whereas the valence band edge derived from Ni 3d orbitals is lowered with increasing $U - J$, the bands derived from O 2p orbitals are unaltered. At the end, the bands gap of NiO_2 increases with increasing $U - J$. In contrast, the lattice constants and characters of the valence and conduction bands of WO_2 do not change upon inclusion of the Coulomb correction term. In Figure 12, are results of our LDA + U

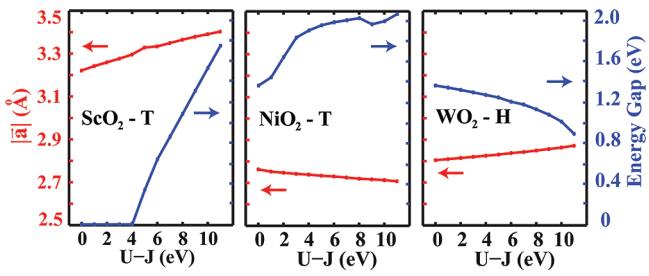

Figure 12. Variations of lattice constants, $|\vec{a}| = |\vec{b}|$, and band gaps of 2D single-layer ScO_2 (in the T structure), NiO_2 (in the T structure), and WO_2 (in the H structure) compounds with $U - J$.

calculations as a function of $U - J$. Apparently, the effect of Coulomb correlation is significant for ScO_2 and NiO_2 having 3d orbitals. However, WO_2, having bands derived from 5d orbitals, is not affected seriously by LDA + U calculations. Because NiO_2 is always nonmagnetic no matter what the value of $U - J$, we would expect the same results when AMF is used. In all $U - J$

dx.doi.org/10.1021/jp212558p | J. Phys. Chem. C 2012, 116, 8983−8999

calculations of ScO_2, we found no fluctuation of the magnetic moment, which maintained a value of 1 μ_B. Our results justify the use of the FFL approximation. Even in the case of the AML approximation, we do not think that the electronic structure of the system will change because the energy shifts in the Sc d orbital bands are not influenced strongly by the variation of $U - J$. The question of whether the stabilities of MO_2 compounds in the H or T structure are affected after LDA + U calculations is addressed by redoing the same phonon calculations with $U - J$ = 4, 8, and 11 eV. The stabilities of these compounds were maintained after LDA + U corrections.

DISCUSSION AND CONCLUSIONS

The unusual properties of graphene, single-layer BN, and MoS_2 discovered in recent studies motivated us to explore 2D single-layer structures of transition-metal oxides and dichalcogenides, MX_2 compounds, in honeycomb-like structure. Three-dimensional crystals of these MX_2 compounds display diverse properties that have been the subject of several studies in the past. Recent studies have shown that 2D flakes of some MX_2 compounds synthesized by various techniques have properties that could be of interest for various nanotechnology applications. MX_2 compounds have a large manifold: Some members of it have layered crystals, such as MoS_2 and graphite, which can allow exfoliation of single layers. We addressed the question of which compounds within this large manifold can form stable and suspended single-layer structures. In particular, we were interested in two honeycomb-like structures, namely, H and T structures. We predicted 52 different individual components that can be stable in either H and/or T structures. Specifically, these compounds can remain stable as free-standing structures, once they are synthesized in one of these single-layer structures. Our predictions were based on state-of-the art first-principles calculations of structure optimization, phonon frequency, molecular dynamics, and mechanical properties. In addition to the extensive stability analysis, we investigated the electronic, magnetic, and mechanical properties of stable compounds. In addition to the optimized lattice constants and internal parameters, we also calculated cohesive energies E_C, formation energies E_f, magnetic moments μ, effective charges on M and X atoms, and in-plane stiffness C. We noted various trends, generally not only in the band gap, but also in cohesive energy and in-plane stiffness (also surface polarities of semiconductors due to charge transfers from M to X), which increase with decreasing row number of X. The lattice constants exhibit a reverse trend. Finally, we found that WO_2 has the highest cohesive energy, highest charge transfer from M to X, and highest in-plane stiffness among MX_2 compounds in this study, suggesting that it is an important single-layer material for future studies.[48]

The calculated band structures reveal electronic properties that could be of interest for future nanoelectronic and sensor applications. For semiconductors, the transition from indirect to direct band gaps with decreasing number of layers has important implications. The surface polarity of semiconductors is another exceptional feature that repulsive interactions are induced quickly as soon as the separation between two parallel layers becomes smaller than the equilibrium distance. Because of their inherent surface polarity, these layers can easily stick to flat substrate surfaces and can be used as coating materials. When coated on flat surfaces as a single layer, they can modify the properties of surfaces dramatically. For example, the polar MoS_2 surface was found to be water-repellant.[52] Our first-principles calculations demonstrate that, in the sliding of two such surfaces, the friction coefficient and the wear are lowered dramatically. In addition, these compounds can attain important functionalities through adatom adsorption (doping) or vacancy defects. In the form of a flake or nanoribbon, MX_2 compounds offer useful electronic and magnetic properties depending on whether edge atoms are saturated by hydrogen. In summary, our results show that single-layer transition-metal dioxides and dichalcogenides in honeycomb-like structures present a variety of physical and chemical properties that could be superior to those of graphene.

AUTHOR INFORMATION

Corresponding Author

*E-mail: ciraci@fen.bilkent.edu.tr.

Notes

The authors declare no competing financial interest.

ACKNOWLEDGMENTS

This work was partially supported by TUBITAK through Grant 108234. S.C. acknowledges the support of TUBA, The Academy of Science of Turkey. Computing resources used in this work were partly provided by the National Center for High Performance Computing of Turkey (UYBHM) under Grant 2-024-2007. Part of the computational resources was provided by TUBITAK ULAKBIM, High Performance and Grid Computing Center (TR-Grid e-Infrastructure). The authors acknowledge fruitful discussions with Professor C. Y. Fong.

REFERENCES

(1) Takada, K.; Sakurai, H.; Takayama-Muromachi, E.; Izumi, F.; Dilanian, R.; Sasaki, T. *Nature* **2003**, *422*, 53−55.
(2) Shishidou, T.; Freeman, A.; Asahi, R. *Phys. Rev. B* **2001**, *64*, 180401.
(3) Lee, C.; Li, Q.; Kalb, W.; Liu, X.-Z.; Berger, H.; Carpick, R. W.; Hone, J. *Science* **2010**, *328*, 76−80.
(4) Reed, C. A.; Cheung, S. K. *Proc, Natl. Acad. Sci. U.S.A.* **1977**, *74*, 1780−1784.
(5) Puthussery, J.; Seefeld, S.; Berry, N.; Gibbs, M.; Law, M. *J. Am. Chem. Soc.* **2011**, *133*, 716−719.
(6) Podberezskaya, N.; Magarill, S.; Pervukhina, N.; Borisov, S. *J. Struct. Chem.* **2001**, *42*, 654−681.
(7) Hwang, H.; Cheong, S. *Science* **1997**, *278*, 1607−1609.
(8) Sims, H.; Oset, S. J.; Butler, W. H.; MacLaren, J. M.; Marsman, M. *Phys. Rev. B* **2010**, *81*, 224436.
(9) Pathak, M.; Sims, H.; Chetry, K. B.; Mazumdar, D.; LeClair, P. R.; Mankey, G. J.; Butler, W. H.; Gupta, A. *Phys. Rev. B* **2009**, *80*, 212405.
(10) Lofwander, T.; Grein, R.; Eschrig, M. *Phys. Rev. Lett.* **2010**, *105*, 207001.
(11) Jin, Y.; Lee, J. *Phys. Rev. B* **2006**, *73*, 064405.
(12) Antonov, V. N.; Andryushchenko, O. V.; Shpak, A. P.; Yaresko, A. N.; Jepsen, O. *Phys. Rev. B* **2008**, *78*, 094409.
(13) Saha, S.; De Raychaudhury, M.; Saha-Dasgupta, T. *Phys. Rev. B* **2008**, *77*, 155428.
(14) Otero-Leal, M.; Rivadulla, F.; Garcia-Hernandez, M.; Pineiro, A.; Pardo, V.; Baldomir, D.; Rivas, J. *Phys. Rev. B* **2008**, *78*, 180415.
(15) Qazilbash, M. M.; Brehm, M.; Chae, B.-G.; Ho, P. C.; Andreev, G. O.; Kim, B.-J.; Yun, S. J.; Balatsky, A. V.; Maple, M. B.; Keilmann, F.; Kim, H.-T.; Basov, D. N. *Science* **2007**, *318*, 1750−1753.
(16) Nguyen, N. T.; Howe, B.; Hash, J. R.; Liebrecht, N.; Zschack, P.; Johnson, D. C. *Chem. Mater.* **2007**, *19*, 1923−1930.
(17) Kamarchuk, G.; Khotkevich, A.; Bagatsky, V.; Ivanov, V.; Molinie, P.; Leblanc, A.; Faulques, E. *Phys. Rev. B* **2001**, *63*, 073107.

(18) Ma, Y.; Dai, Y.; Guo, M.; Niu, C.; Zhu, Y.; Huang, B. *ACS Nano* **2012**, *6*, 1695−1701.
(19) Alfonso, D. R. *J. Phys. Chem. C* **2010**, *114*, 8971−8980.
(20) Blanchard, M.; Alfredsson, M.; Brodholt, J.; Price, G.; Wright, K.; Catlow, C. *J. Phys. Chem. B* **2005**, *109*, 22067−22073.
(21) Eyert, V.; Hock, K.; Fiechter, S.; Tributsch, H. *Phys. Rev. B* **1998**, *57*, 6350−6359.
(22) Bostick, B.; Fendorf, S.; Bowie, B.; Griffiths, P. *Environ. Sci. Technol.* **2000**, *34*, 1494−1499.
(23) Bruggeman, C.; Maes, N. *Environ. Sci. Technol.* **2010**, *44*, 4210−4216.
(24) Gao, P.; Xie, Y.; Ye, L.; Chen, Y.; Guo, Q. *Cryst. Growth Des.* **2006**, *6*, 583−587.
(25) Barnard, A. S.; Russo, S. P. *J. Phys. Chem. C* **2007**, *111*, 11742−11746.
(26) Hu, Y.; Zheng, Z.; Jia, H.; Tang, Y.; Zhang, L. *J. Phys. Chem. C* **2008**, *112*, 13037−13042.
(27) Novoselov, K.; Geim, A.; Morozov, S.; Jiang, D.; Zhang, Y.; Dubonos, S.; Grigorieva, I.; Firsov, A. *Science* **2004**, *306*, 666−669.
(28) Geim, A. K.; Novoselov, K. S. *Nat. Mater.* **2007**, *6*, 183−191.
(29) Durgun, E.; Tongay, S.; Ciraci, S. *Phys. Rev. B* **2005**, *72*, 075420.
(30) Cahangirov, S.; Topsakal, M.; Akturk, E.; Şahin, H.; Ciraci, S. *Phys. Rev. Lett.* **2009**, *102*, 236804.
(31) Şahin, H.; Cahangirov, S.; Topsakal, M.; Bekaroglu, E.; Akturk, E.; Senger, R. T.; Ciraci, S. *Phys. Rev. B* **2009**, *80*, 155453.
(32) Aufray, B.; Kara, A.; Vizzini, S.; Oughaddou, H.; Léandri, C.; Ealet, B.; Le Lay, G. *Appl. Phys. Lett.* **2010**, *96*, 183102.
(33) Jin, C.; Lin, F.; Suenaga, K.; Iijima, S. *Phys. Rev. Lett.* **2009**, *102*, 195505.
(34) Mak, K. F.; Lee, C.; Hone, J.; Shan, J.; Heinz, T. F. *Phys. Rev. Lett.* **2010**, *105*, 136805.
(35) Wang, Z.; Zhao, K.; Li, H.; Liu, Z.; Shi, Z.; Lu, J.; Suenaga, K.; Joung, S.-K.; Okazaki, T.; Jin, Z.; Gu, Z.; Gao, Z.; Iijima, S. *J. Mater. Chem.* **2011**, *21*, 171−180.
(36) Novoselov, K.; Jiang, D.; Schedin, F.; Booth, T.; Khotkevich, V.; Morozov, S.; Geim, A. *Proc. Natl. Acad. Sci. U.S.A.* **2005**, *102*, 10451−10453.
(37) Li, T.; Galli, G. *J. Phys. Chem. C* **2007**, *111*, 16192−16196.
(38) Li, Y.; Zhou, Z.; Zhang, S.; Chen, Z. *J. Am. Chem. Soc.* **2008**, *130*, 16739−16744.
(39) Lebègue, S.; Eriksson, O. *Phys. Rev. B* **2009**, *79*, 115409.
(40) Splendiani, A.; Sun, L.; Zhang, Y.; Li, T.; Kim, J.; Chim, C.-Y.; Galli, G.; Wang, F. *Nano Lett.* **2010**, *10*, 1271−1275.
(41) Ataca, C.; Şahin, H.; Akturk, E.; Ciraci, S. *J. Phys. Chem. C* **2011**, *115*, 3934−3941.
(42) Ataca, C.; Ciraci, S. *J. Phys. Chem. C* **2011**, *115*, 13303−13311.
(43) Ataca, C.; Topsakal, M.; Akturk, E.; Ciraci, S. *J. Phys. Chem. C* **2011**, *115*, 16354−16361.
(44) Liu, L.; Kumar, S. B.; Ouyang, Y.; Guo, J. *IEEE Trans. Electron Devices* **2011**, *58*, 3042−3047.
(45) Kuc, A.; Zibouche, N.; Heine, T. *Phys. Rev. B* **2011**, *83*, 245213.
(46) Lee, C.; Yan, H.; Brus, L. E.; Heinz, T. F.; Hone, J.; Ryu, S. *ACS Nano* **2010**, *4*, 2695−2700.
(47) Matte, H. S. S. R.; Gomathi, A.; Manna, A. K.; Late, D. J.; Datta, R.; Pati, S. K.; Rao, C. N. R. *Angew. Chem., Int. Ed.* **2010**, *49*, 4059−4062.
(48) Cahangirov, S.; Ataca, C.; Topsakal, M.; Şahin, H.; Ciraci, S. *Phys. Rev. Lett.* **2012**, *108*, 126103.
(49) Hinnemann, B.; Moses, P.; Bonde, J.; Jorgensen, K.; Nielsen, J.; Horch, S.; Chorkendorff, I.; Norskov, J. *J. Am. Chem. Soc.* **2005**, *127*, 5308−5309.
(50) Moses, P. G.; Hinnemann, B.; Topsoe, H.; Norskov, J. K. *J. Catal.* **2007**, *248*, 188−203.
(51) Kline, G.; Kam, K.; Ziegler, R.; Parkinson, B. *Solar Energy Mater.* **1982**, *6*, 337−350.
(52) To be published elsewhere.
(53) Radisavljevic, B.; Radenovic, A.; Brivio, J.; Giacometti, V.; Kis, A. *Nat. Nanotechnol.* **2011**, *6*, 147−150.
(54) Coleman, J. N.; Coleman, J. N.; Lotya, M.; O'Neill, A.; Bergin, S. D.; King, P. J.; Khan, U.; Young, K.; Gaucher, A.; De, S.; Smith, R. J.; Shvets, I. V.; Arora, S. K.; Stanton, G.; Kim, H.-Y.; Lee, K.; Kim, G. T.; Duesberg, G. S.; Hallam, T.; Boland, J. J.; Wang, J. J.; Donegan, J. F.; Grunlan, J. C.; Moriarty, G.; Shmeliov, A.; Nicholls, R. J.; Perkins, J. M.; Grieveson, E. M.; Theuwissen, K.; McComb, D. W.; Nellist, P. D.; Nicolosi, V. *Science* **2011**, *331*, 568−571.
(55) *Landolt−Bornstein Database*; Springer: New York, 2010.
(56) Ding, Y.; Wang, Y.; Ni, J.; Shi, L.; Shi, S.; Tang, W. *Physica B: Condens. Matter* **2011**, *406*, 2254−2260.
(57) De Padova, P.; Quaresima, C.; Olivieri, B.; Perfetti, P.; Le Lay, G. *Appl. Phys. Lett.* **2011**, *98*, 081909.
(58) Aufray, B.; Kara, A.; Vizzini, S.; Oughaddou, H.; Leandri, C.; Ealet, B.; Le Lay, G. *Appl. Phys. Lett.* **2010**, *96*, 183102.
(59) Houssa, M.; Pourtois, G.; Afanas'ev, V. V.; Stesmans, A. *Appl. Phys. Lett.* **2010**, *97*, 112106.
(60) Lalmi, B.; Oughaddou, H.; Enriquez, H.; Kara, A.; Vizzini, S.; Ealet, B.; Aufray, B. *Appl. Phys. Lett.* **2010**, *97*, 223109.
(61) De Padova, P.; Quaresima, C.; Ottaviani, C.; Sheverdyaeva, P. M.; Moras, P.; Carbone, C.; Topwal, D.; Olivieri, B.; Kara, A.; Oughaddou, H.; Aufray, B.; Le Lay, G. *Appl. Phys. Lett.* **2010**, *96*, 261905.
(62) Bekaroglu, E.; Topsakal, M.; Cahangirov, S.; Ciraci, S. *Phys. Rev. B* **2010**, *81*, 075433.
(63) Topsakal, M.; Cahangirov, S.; Bekaroglu, E.; Ciraci, S. *Phys. Rev. B* **2009**, *80*, 235119.
(64) Tusche, C.; Meyerheim, H. L.; Kirschner, J. *Phys. Rev. Lett.* **2007**, *99*, 026102.
(65) Wang, L.; Chen, K.; Dong, L. *J. Phys. Chem. C* **2010**, *114*, 17358−17361.
(66) Blochl, P. *Phys. Rev. B* **1994**, *50*, 17953−17979.
(67) Ceperley, D.; Alder, B. *Phys. Rev. Lett.* **1980**, *45*, 566−569.
(68) Perdew, J.; Chevary, J.; Vosko, S.; Jackson, K.; Pederson, M.; Singh, D.; Fiolhais, C. *Phys. Rev. B* **1992**, *46*, 6671−6687.
(69) Grimme, S. *J. Comput. Chem.* **2006**, *27*, 1787−1799.
(70) Bucko, T.; Hafner, J.; Lebegue, S.; Angyan, J. G. *J. Phys. Chem. A* **2010**, *114*, 11814−11824.
(71) Dudarev, S.; Botton, G.; Savrasov, S.; Humphreys, C.; Sutton, A. *Phys. Rev. B* **1998**, *57*, 1505−1509.
(72) Monkhorst, H. J.; Pack, J. D. *Phys. Rev. B* **1976**, *13*, 5188−5192.
(73) Henkelman, G.; Arnaldsson, A.; Jonsson, H. *Comput. Mater. Sci.* **2006**, *36*, 354−360.
(74) Heyd, J.; Scuseria, G.; Ernzerhof, M. *J. Chem. Phys.* **2003**, *118*, 8207−8215.
(75) Fuchs, F.; Furthmueller, J.; Bechstedt, F.; Shishkin, M.; Kresse, G. *Phys. Rev. B* **2007**, *76*, 115109.
(76) Shishkin, M.; Kresse, G. *Phys. Rev. B* **2006**, *74*, 035101.
(77) Kresse, G.; Hafner, J. *Phys. Rev. B* **1993**, *47*, 558−561.
(78) Kresse, G.; Furthmuller, J. *Phys. Rev. B* **1996**, *54*, 11169−11186.
(79) Alfe, D. *Comput. Phys. Commun.* **2009**, *180*, 2622−2633.
(80) Giannozzi, P.; Baroni, S.; Bonini, N.; Calandra, M.; Car, R.; Cavazzoni, C.; Ceresoli, D.; Chiarotti, G. L.; Cococcioni, M.; Dabo, I.; Corso, A. D.; Gironcoli, S.; Fabris, S.; Fratesi, G.; Gebauer, R.; Gerstmann, U.; Gougoussis, C.; Kokalj, A.; Lazzeri, M.; Martin-Samos, L.; Marzari, N.; Mauri, F.; Mazzarello, R.; Paolini, S.; Pasquarello, A.; Paulatto, L.; Sbraccia, C.; Scandolo, S.; Sclauzero, S.; Seitsonen, A. P.; Smogunov, A.; Umari, P.; Wentzcovitch, R. M. *J. Phys. Condens. Matter* **2009**, *21*, 395502.
(81) Cohesive energies of constituent elements, M and X, in their equilibrium state taken from: Kittel, C. *Introduction to Solid State Physics*, 7th ed.; Wiley: New York, 1996.
(82) Imai, H.; Shimakawa, Y.; Kubo, Y. *Phys. Rev. B* **2001**, *64*, 241104.
(83) Jaswal, S. S. *Phys. Rev. B* **1979**, *20*, 5297−5300.
(84) Strocov, V. N.; Krasovskii, E. E.; Schattke, W.; Barrett, N.; Berger, H.; Schrupp, D.; Claessen, R. *Phys. Rev. B* **2006**, *74*, 195125.
(85) Oka, Y.; Sato, S.; Yao, T.; Yamamoto, N. *J. Solid State Chem.* **1998**, *141*, 594−598.

(86) Mulazzi, M.; Chainani, A.; Katayama, N.; Eguchi, R.; Matsunami, M.; Ohashi, H.; Senba, Y.; Nohara, M.; Uchida, M.; Takagi, H.; Shin, S. *Phys. Rev. B* **2010**, *82*, 075130.
(87) van Landuyt, J.; Wiegers, G. A.; Amelinckx, S. *Phys. Status Solidi (a)* **1978**, *46*, 479−492.
(88) Woolley, A. M.; Wexler, G. *J. Phys. C: Solid State Phys.* **1977**, *10*, 2601.
(89) Vinokurov, A. A.; Tyurin, A. V.; Emelina, A. L.; Gavrichev, K. S.; Zlomanov, V. P. *Inorg. Mater.* **2009**, *45*, 480−485.
(90) Kulatov, E.; Mazin, I. *J. Phys.: Condens. Matter* **1990**, *2*, 343−350.
(91) Fang, C.; vanBruggen, C.; deGroot, R.; Wiegers, G.; Haas, C. *J. Phys.: Condens. Matter* **1997**, *9*, 10173−10184.
(92) Devaraj, S.; Munichandraiah, N. *J. Phys. Chem. C* **2008**, *112*, 4406−4417.
(93) Tappero, R.; Baraille, I.; Lichanot, A. *Phys. Rev. B* **1998**, *58*, 1236−1242.
(94) Vogt, H.; Chattopadhyay, T.; Stolz, H. *J. Phys. Chem. Solids* **1983**, *44*, 869−873.
(95) Chattopadhyay, T.; Vonschnering, H.; Stansfield, R.; Mcintyre, G. *Z. Kristallogr.* **1992**, *199*, 13−24.
(96) Hastings, J. M.; Elliott, N.; Corliss, L. M. *Phys. Rev.* **1959**, *115*, 13−17.
(97) Peng, Q.; Dong, Y.; Deng, Z.; Kou, H.; Gao, S.; Li, Y. *J. Phys. Chem. B* **2002**, *106*, 9261−9265.
(98) Vulliet, P.; Sanchez, J.; Braithwaite, D.; Amanowicz, M.; Malaman, B. *Phys. Rev. B* **2001**, *63*, 184403.
(99) Ouertani, B.; Ouerfelli, J.; Saadoun, M.; Bessais, B.; Ezzaouia, H.; Bernede, J. *Solar Energy Mater. Solar Cells* **2005**, *87*, 501−511.
(100) Kjekshus, A.; Rakke, T.; F., A. A. *Acta Chem. Scand.* **1974**, *28a*, 996−1000.
(101) Pertlik, F. *Anz. Osterr. Akad. Wiss., Math.-Naturwiss. Kl.* **1986**, *123*, 123.
(102) Brostigen, G.; Kjekshus, A. *Acta Chem. Scand.* **1970**, *24*, 1925−1940.
(103) Seguin, L.; Amatucci, G.; Anne, M.; Chabre, Y.; Strobel, P.; Tarascon, J.; Vaughan, G. *J. Power Sources* **1999**, *81*, 604−606.
(104) Chen, X.; Fan, R. *Chem. Mater.* **2001**, *13*, 802−805.
(105) Carmalt, C.; Manning, T.; Parkin, I.; Peters, E.; Hector, A. *J. Mater. Chem.* **2004**, *14*, 290−291.
(106) Guillamon, I.; Suderow, H.; Vieira, S.; Cario, L.; Diener, P.; Rodiere, P. *Phys. Rev. Lett.* **2008**, *101*, 166407.
(107) Yokoya, T.; Kiss, T.; Chainani, A.; Shin, S.; Nohara, M.; Takagi, H. *Science* **2001**, *294*, 2518−2520.
(108) Campagnoli, G.; Gustinetti, A.; Stella, A. *J. Phys. C: Solid State Phys.* **1974**, *7*, L223.
(109) Battaglia, C.; Cercellier, H.; Clerc, F.; Despont, L.; Garnier, M.; Koitzsch, C.; Aebi, P.; Berger, H.; Forro, L.; Ambrosch-Draxl, C. *Phys. Rev. B* **2005**, *72*, 195114.
(110) Moosburger-Will, J.; Kuendel, J.; Klemm, M.; Horn, S.; Hofmann, P.; Schwingenschloegl, U.; Eyert, V. *Phys. Rev. B* **2009**, *79*, 115113.
(111) Scanlon, D. O.; Watson, G. W.; Payne, D. J.; Atkinson, G. R.; Egdell, R. G.; Law, D. S. L. *J. Phys. Chem. C* **2010**, *114*, 4636−4645.
(112) Du, G.; Guo, Z.; Wang, S.; Zeng, R.; Chen, Z.; Liu, H. *Chem. Commun.* **2010**, *46*, 1106−1108.
(113) Dungey, K.; Curtis, M.; Penner-Hahn, J. *Chem. Mater.* **1998**, *10*, 2152−2161.
(114) Morales, J.; Santos, J.; Tirado, J. *Solid State Ionics* **1996**, *83*, 57−64.
(115) Towle, L. C.; Oberbeck, V.; Brown, B. E.; Stajdohar, R. E. *Science* **1966**, *154*, 895−896.
(116) Jones, F.; Egdell, R.; Brown, A.; Wondre, F. *Surf. Sci.* **1997**, *374*, 80−94.
(117) Heising, J.; Kanatzidis, M. *J. Am. Chem. Soc.* **1999**, *121*, 638−643.
(118) Feldman, Y.; Frey, G.; Homyonfer, M.; Lyakhovitskaya, V.; Margulis, L.; Cohen, H.; Hodes, G.; Hutchison, J.; Tenne, R. *J. Am. Chem. Soc.* **1996**, *118*, 5362−5367.
(119) Straub, T.; Fauth, K.; Finteis, T.; Hengsberger, M.; Claessen, R.; Steiner, P.; Hufner, S.; Blaha, P. *Phys. Rev. B* **1996**, *53*, 16152−16155.
(120) Mar, A.; Jobic, S.; Ibers, J. *J. Am. Chem. Soc.* **1992**, *114*, 8963−8971.
(121) Before one decides that a given compound is not stable, one has to make every effort to vary specific parameters of the calculations. First, if a given compound is magnetic, spin-polarized calculations have to be carried out. In some cases, distant neigbors have to be taken into account. Calculations with relatively small superlattices might end up with instability. In other cases, it might be essential to use the correct FTT mesh to avoid ending up with fake instability. Briefly, even though phonon calculations provide a rigorous test, one has to be sure that appropriate parameters are used.
(122) Liu, C.-C.; Feng, W.; Yao, Y. *Phys. Rev. Lett.* **2011**, *107*, 076802.
(123) De Padova, P.; Quaresima, C.; Olivieri, B.; Perfetti, P.; Le Lay, G. *J. Phys. D: Appl. Phys.* **2011**, *44*, 312001.
(124) Kohn, W. *Phys. Rev. Lett.* **1959**, *2*, 393−394.
(125) Kam, K.; Parkinson, B. *J. Phys. Chem.* **1982**, *86*, 463−467.
(126) Şahin, H.; Topsakal, M.; Ciraci, S. *Phys. Rev. B* **2011**, *83*, 115432.
(127) Nair, R. R.; Ren, W.; Jalil, R.; Riaz, I.; Kravets, V. G.; Britnell, L.; Blake, P.; Schedin, F.; Mayorov, A. S.; Yuan, S.; Katsnelson, M. I.; Cheng, H.-M.; Strupinski, W.; Bulusheva, L. G.; Okotrub, A. V.; Grigorieva, I. V.; Grigorenko, A. N.; Novoselov, K. S.; Geim, A. K. *Small* **2010**, *6*, 2877−2884.
(128) Şahin, H.; Ataca, C.; Ciraci, S. *Appl. Phys. Lett.* **2009**, *95*, 222510.
(129) Ylvisaker, E. R.; Pickett, W. E.; Koepernik, K. *Phys. Rev. B* **2009**, *79*, 035103.